IDEA League

MASTER OF SCIENCE IN APPLIED GEOPHYSICS

RESEARCH THESIS

Surface Wave Analysis for the characterization of granular material deposits

Tahira Nicole Ashruf

August 7, 2015

Surface Wave Analysis for the characterization of granular material deposits

MASTER OF SCIENCE THESIS

for the degree of Master of Science in Applied Geophysics at

Delft University of Technology

ETH Zürich

RWTH Aachen University

by

Tahira Nicole Ashruf

August 7, 2015

Department of Geoscience & Engineering	·	Delft University of Technology
Department of Earth Sciences	·	ETH Zürich
Faculty of Georesources and Material Engineering	·	RWTH Aachen University

August 7, 2015

Delft University of Technology

Printed in The Netherlands, Switzerland, Germany

IDEA LEAGUE
JOINT MASTER'S IN APPLIED GEOPHYSICS

Delft University of Technology, The Netherlands
ETH Zürich, Switzerland
RWTH Aachen, Germany

Dated: *August 7, 2015*

Supervisor(s):

Dr. Laura Valentina Socco

Dr. Ranajit Ghose

Committee Members:

Dr. Laura Valentina Socco

Dr. Ranajit Ghose

Prof. Jan van der Kruk

Abstract

Knowledge of near-surface seismic-wave velocity of granular materials plays a valuable role in seismic exploration data processing. I will use the surface-wave analysis method for estimation of shear-wave velocity profile and P-wave refraction for estimation of pressure-wave velocity on a data set acquired over a sand dune in The Netherlands, a dune area part of The Holland coast. For surface-wave analysis I exploit the fact that in these materials the velocity profile follows a power-law and I invert for the power-law coefficients using a Monte Carlo inversion. A second power-law is introduced into the Monte Carlo inversion to recover vertically varying structures. The P-wave refraction is applied for estimation of the groundwater depth and P-wave velocity. After the seismic data were acquired, several analyses were made on the extracted dispersion curves from different sources, windowing in space domain indicate the presence of lateral variation. The estimated shear-wave velocity profiles demonstrates the usefulness of imposing a power-law trend to the velocity. Although the inverted power-law coefficients results into small differences with the literature and theoretical values, these can be explained by the varying shapes of the grains. Furthermore, the implementation of the second power-law results into velocities that are lower than the first layer. The depth of the shear-wave velocity profiles is limited by the shallow position of the water-table around 3 m. For the best practice in field work the vibroseis source is advised due to the advantage of the continuous sweep covering the whole frequency band in one signal.

Acknowledgements

I want to start thanking Valentina Socco for her critical supervision and always being available to share her knowledge with me. Secondly, to Ranajit Ghose for the huge help during the fieldwork and the supervision. To Flora Garofalo for her patient and useful tips regarding the Matlab codes. To Alber Hemstede for the technical help during the fieldwork.

The last six months were in a completely new environment and to the people who I can call my "Italian family" now, I am very thankful. To Allesandro Arato who was always available for general questions regarding the thesis and Diego for the technical support. To Family Scavone and Marco Dattilo for making me feel at home and the emotional support during difficult moments throughout the research project.

Last but not least, I want to thank my family and friends who has supported me the last three years in Europe for always motivating me to never give up on my dreams.

Delft University of Technology — Tahira Nicole Ashruf
August 7, 2015

Table of Contents

Abstract **vii**

Acknowledgements **ix**

1 Introduction **1**

1-1 Characterizing loose granular materials 1

1-2 Thesis objectives and outline 3

2 Theory and Method **5**

2-1 Loose granular material 5

  2-1-1 Guided surface acoustic modes 7

2-2 Surface-wave analysis 9

  2-2-1 Acquisition 10

  2-2-2 Processing 11

  2-2-3 Inversion 12

2-3 Refraction travel-time inversion 13

3 Field Experiment **15**

3-1 Experimental site 15

3-2 Acquisition 18

4 Processing and Inversion results 23
- 4-1 Processing 23
  - 4-1-1 Frequency range investigation 27
  - 4-1-2 F-k domain stacking 33
  - 4-1-3 Lateral variation investigation 35
- 4-2 Inversion 39
  - 4-2-1 Position of the water-table 40
  - 4-2-2 Estimation of a preliminary value of alpha 43
  - 4-2-3 Shear-wave velocity profile 47

5 Discussion 56

6 Conclusions 59
- 6-1 Conclusions 59
- 6-2 Outlook 60

Bibliography 62

List of Figures

2-1 Representation of multimodal behavior 8
2-2 Representation of geometric dispersion 9
2-3 Principle of P-wave refraction 14

3-1 Map of the Netherlands with site location 16
3-2 Google image of the study area 17
3-3 Picture of the field set up 18
3-4 Illustration of the survey geometry 19
3-5 Examples of raw data 21

4-1 Workflow of the processing steps 24
4-2 F-K domain of acquisition line 1 28
4-3 Dispersion curves of acquisition line 1; Δx = 0.20 m 29
4-4 Dispersion curves of acquisition line 1; Δx = 0.30 m 29
4-5 F-K domain of acquisition line 2; Δx = 0.25 m 31
4-6 Dispersion curves of acquisition line 2; Δx = 0.25 m 32
4-7 Stacking results f-k domain and dispersion curve 34
4-8 Dispersion curves of different shots line 1; Δx = 0.30 m 35
4-9 Dispersion curves of different shots line 2; Δx = 0.25 m 36
4-10 Gaussian windowing results 37
4-11 Dispersion curves with varying window lengths 38
4-12 Workflow of the inversion 39
4-13 Travel-time versus offset 41

4-14 Data points different layers . . . 41
4-15 Inverted depth refracted layer . . . 42
4-16 Alpha of vibroseis stack line 1 . . . 44
4-17 Alpha of the second portion . . . 45
4-18 Alpha of weight drop line 2 . . . 46
4-19 Inversion results line 1 . . . 50
4-20 Inversion results line 2 . . . 51
4-21 Inversion results second layer line 1 . . . 54
4-22 Results misfit second layer line 1 . . . 55

List of Tables

2-1 Seismic-wave velocity and density 6

3-1 Field acquisition and recording parameters 20

4-1 Processing record of line 1; Δx=0.20 m 25
4-2 Processing record of line 1; $\Delta x = 0.30$ m 26
4-3 Processing record of line 2; $\Delta x = 0.25$ m 27
4-4 Results of the travel-time inversion 40
4-5 Preliminary alpha estimation results 44
4-6 Input parameters Monte Carlo Inversion 48
4-7 Inverted power-law coefficients 49
4-8 Parameters of the second layer 53

Chapter 1

Introduction

1-1 Characterizing loose granular materials

Granular materials, such as soils, form mainly the weathering layer below the ground surface. This weathering layer is generally a few meters to several tens of meters thick of abnormally low seismic velocity. Although it may only be a few meters thick, they can severely effect the quality of reflection data (Liner 2007), especially when strong lateral variations in the thickness or velocity exist (Robinson and Al-Husseini 1982). Knowledge of the near-surface seismic-wave velocity of granular deposits is therefore of great importance for static corrections applied to geophysical data, particularly seismic data.

Among the available seismic methods for subsurface characterization, surface-wave analysis has widely been adopted as a very powerful tool for applications in near-surface velocity characterizations (Socco et al. 2010). Surface waves are interesting because they are capable of resolving subsurface features at scales of tens to hundreds of meters laterally and vertically. The method uses the geometric dispersion of surface waves traveling through a non-homogeneous medium, which contains valuable information on the shear-wave velocity of the medium (Gabriels et al. 1987).

Although in granular materials these surface-wave modes are called guided surface acoustic modes (GSAM), instead of Rayleigh waves (Aleshin et al. 2007). Nevertheless, the surface-wave analysis can also be applied on other kinds of guided waves and not only on surface waves (Socco et al. 2010). In addition to the inversion of the surface-wave method, the presence and position of the water table is important to know due to abrupt changes of the properties at the water table (Foti 2002).

In unconsolidated granular layers, the velocity profiles are related to a power-law which is dependent on overburden pressure (Gassmann 1951). For each profile the compressional wave velocity (V_p) and shear-wave velocity (V_s) are controlled by γ_p and γ_s are depth-independent coefficients mainly related to the elastic properties of the grains for V_p and V_s respectively, and α_p and α_s are the power-law exponents for V_p and V_s respectively. This velocity profile trend can be used to invert surface wave data by imposing a power-law trend to the shear-wave velocity and estimating the power-law coefficients. In addition, Bergamo et al. (2013) shows that also compressional-wave velocity models can be inferred from the surface wave inversion if higher surface-wave modes are retrieved.

Various studies used the surface-wave analysis for characterizating granular material by assuming a stack of linear elastic homogeneous layers to the velocity. Yet, few studies has applied the concept of imposing a power-law trend to the field data of granular deposits. In previous work this concept is applied on laboratory scale (Bodet et al. 2010; Bergamo et al. 2014) and on synthetic data by Bergamo et al. (2013). Furthermore, Bergamo et al. (2014) created a velocity profile of two layers by imposing the power-law trend to the velocity of both the layers. However, this method does not account for the density of the layer above and the interface depth.

1-2 Thesis objectives and outline

In this experimental study, the goal is to characterize granular materials and provide recommendations on the best practice in field work. To characterize granular materials, I will retrieve the near-surface velocity model and power-law coefficients by applying the concept of the power-law trend to the inversion step of the surface-wave analysis. For the second layer, I will retrieve the velocity profile by imposing a power-law which includes the density of both layers and the interface depth. To provide recommendations for the best field work practice, I will investigate the frequency range by comparing the f-k domain and dispersion curves taken from different sources. Seismic data are acquired with impulsive sources and vibroseis with different sweeps, along two acquisition lines. The acquisition was carried out on a sand dune in Wassenaar, The Netherlands. The processing of the seismic data was performed at Politechnico di Torino, Italy.

I will start the thesis in chapter 2 with the theory on granular materials and how the properties will be exploited. In chapter 3, I explain the study area and the field acquisition parameters along the two acquisition lines with different spatial sampling.

I will investigate the frequency range of the processed dispersion curves in section 4-1-1. In section 4-1-2, I will perform stacking in the f-k domain from different seismic sources to improve the lateral resolution. Followed by investigating the lateral variation in section 4-1-3 using the Gaussian windowing technique. In section 4-2-1, I will show the estimated water-table position from P-wave refraction. Before starting the inversion, the power-law coefficient alpha will be first estimated in section 4-2-2. In the end, I will compute the shear-wave velocity profiles and power-law coefficients in section 4-2-3.

In section 5, I discuss the results of the surface-wave analysis and P-wave refraction. Finally in chapter 6, I present the conclusions of this experimental study and outlook for future research focusing on further improvements for characterizing sand deposits.

Chapter 2

Theory and Method

I start off by explaining the behavior of seismic properties in loose granular material. Followed by some literature values of the seismic properties and the corresponding parameters. Afterwards, I explain the method for characterization of these properties through surface-wave analysis. In the end, the P-wave refraction method is briefly described for calaculation of the water-table position.

2-1 Loose granular material

Granular materials, such as soils, form mainly the weathering layer below the ground surface. This weathering layer is generally a heterogeneous layer of loose granular medium and is a few meters to several tens of meters thick of abnormally low seismic velocity. The seismic properties, compressional- and shear-wave propagation velocity ($V_{p,s}$) of unconsolidated granular materials depend on overburden pressure (Gassmann 1951). The power-law dependency of $V_{p,s}$ on pressure is given by:

$$V_{p,s} = \gamma_{p,s}(\rho g z)^{\alpha_{p,s}} \tag{2-1}$$

where g is the acceleration due to gravity, z is depth, $\gamma_{p,s}$ is a depth-independent coefficient mainly depending on elastic properties of grains, and $\alpha_{p,s}$ is the power-law exponent for shear-waves. This gravity-induced rigidity gradient in combination with the free surface evolves into the propagation of dispersive, guided surface acoustic modes along the surface with low velocity (Aleshin et al. 2007). The guided surface acoustic modes are further explained in section 2-1-1. Table 2-1 presents some literature values of wave velocity and density.

According to experimental studies on unconsolidated sands by Zimmer et al. (2006), the shear-wave velocity exhibits a pressure dependence approximately proportional to the fourth root of the effective pressure $p'^{\frac{1}{4}}$. Theoretical formulations based on contact theory of perfect spheres with equal size, predict a pressure dependence of one-sixth power $p'^{\frac{1}{6}}$ (Walton 1987). In contrast, the empirical values vary from one-third to one-sixth $p'^{\frac{1}{3}}$ - $p'^{\frac{1}{6}}$. These differences are due to different compaction due to loading or to the varying shape of the grains.

Table 2-1: Seismic-wave velocity and density values for unconsolidated sand and wet sand. These values are based on the literature, with the references in the last column.

	Compressional-wave V_p (m/s)	Shear-wave V_s (m/s)	Density ρ (kg/m^3)	
Unconsolidated sand	100 - 300	60 - 180	1500 - 1900	(Bachrach et al. 2000) (Santamarina et al. 2001)
Wet sand	1500 - 2000	400 - 600	1900 - 2100	(Mavko 2005)

Furthermore, the compressional- and shear-wave propagation velocity ($V_{p,s}$) are related to the Poisson's ration. The Poisson's ratio σ is an useful parameter, since laboratory evidence indicates that it will identify whether pores in loose granular materials are dry or fluid saturated (Rossow et al. 1983). The small-strain value of Poisson's ratio σ can be obtained from V_p and V_s:

$$\sigma = \frac{(\frac{V_p}{V_s})^2 - 2}{2(\frac{V_p}{V_s})^2 - 2} \tag{2-2}$$

Poisson's ratio σ for unsaturated granular media at small strains and constant fabric is very small, and values lower than 0.15 is expected. If the medium is fluid or a saturated soil, then σ reaches 0.5, due to $V_p/V_s \rightarrow \infty$(Santamarina et al. 2001).

2-1-1 Guided surface acoustic modes

The guided surface acoustic modes GSAM, divided into shear horizontal SH waves and vertical plane waves P+SV, are characterized by an infinite number of surface-wave modes, while in the homogeneous solids only one surface P+SV mode exist (Aleshin et al. 2007). The dispersion relation derived by Aleshin et al. (2007) explains the geometrical dispersion of surface modes propagation. The geometrical dispersion shown in figure 2-1 is the variation of wave propagation velocity with frequency caused by wave-material interaction phenomena or by the geometry of the medium (Socco and Strobbia 2004). This dispersion relation is useful for the inversion of the experimental data, i.e. in order to retrieve near-surface information from measurements of the dispersion relations of the localized modes (Aleshin et al. 2007). It has been proven that the multimodal phenomenon can be analyzed as they were Rayleigh waves in a layered media with fine layers simulating a vertical stiffness (velocity gradient). The geometric dispersion of Rayleigh waves are shown in figure 2-2 (Socco et al. 2010).

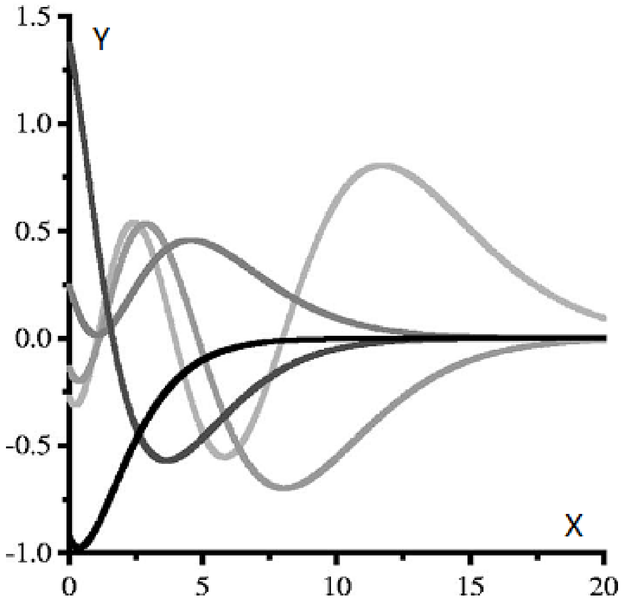

Figure 2-1: Representation of the P-SV modes displacement along the y-axes and the displacement in depth along the x-axis, describing the multimodal behavior (Aleshin et al. 2007).

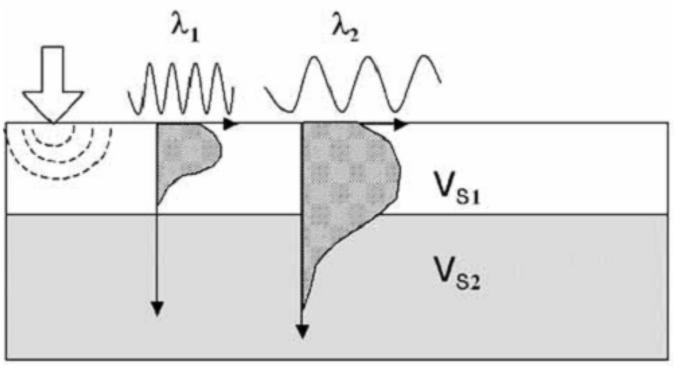

Figure 2-2: Schematic representation of geometric dispersion of Rayleigh waves: different wavelengths (λ_1, λ_2) of the surface wave behaviors, investigating different layers resulting in different velocities (V_{s1}, V_{s2}) depending on the elastic property (Socco and Strobbia 2004) .

2-2 Surface-wave analysis

Surface-wave analysis uses the geometric dispersion, in section 2-1-1, of surface waves to infer the properties of the medium by identifying the modal parameters (Socco et al. 2010). This is done by estimating experimental dispersion curves from the field data and solving the inverse problem for building the near-surface shear-wave velocity V_s models. The standard processing for surface-wave analysis is divided into the following steps:

1. Acquisition

2. Processing

3. Inversion

2-2-1 Acquisition

Acquisition is subdivided into passive and active tests. The passive acquisition is often related to seismological and earthquake engineering. Here an active multichannel approach is adopted based on linear arrays of geophones (Park et al. 1999) to better sample the surface wave propagation in space and time and adopting acquisition parameters that fulfill surface wave requirements (Socco and Boiero 2008). The goal of the acquisition is to gather data that have a high S/N over a wide frequency band, allowing for modal separation and recognition, separation and filtering out of coherent noise, and estimation of uncertainties (Socco and Boiero 2008).

Improvement of modal separation depends on the array length that affects the wavenumber resolution Δk. Long arrays should improve the modal separation but are therefore more sensitive to lateral variations, affecting the S/N ratio and high-frequency attenuation (Foti et al. 2014). The receiver spacing Δx influences the maximum wavenumber k_{max} and the shortest possible detectable wavelength $\lambda_{min} = 2 \times \Delta x$.

For the source-offset, there are two aspects explained by Park et al. (1999) to be taken into consideration: near-field effects and far-offset effects. The latter refers to the contamination of body waves because of attenuation of high-frequency ground roll at longer offsets. Near-field effects refer to the lack of linear coherency in phase at lower frequencies, because plane-wave propagation of surface waves occurs when the near-offset is greater than half the maximum desired wavelength λ_{max} (Stokoe et al. 1994).

The time sampling is chosen, depending on the highest frequency that will be acquired according to the Nyquist sampling theorem (Socco and Boiero 2008). The time-window needs to be long enough to record on all the traces the whole surface wave.

The equipment has effect on the produced and recorded frequency. Impulsive sources, depending on the weight has their energy concentrated in the low or high frequency band (Foti et al. 2014). For heavier impulsive sources the energy lies more in the low frequency band. While the advantage of the vibrating sources are the continuous sweeps that cover the whole frequency band in a single signal (Foti et al. 2014). The natural frequency of the geophones gives an indication of the minimum detectable frequency.

2-2-2 Processing

One of the main steps in surface-wave analysis is extraction of dispersion curves. For the extraction of the dispersion curves several wavefield transforms can be used ($\omega - p$ or $f - k$). In this work, I have extracted the dispersion curves by transforming the experimental data from the space-time (x-t) domain to the frequency-wavenumber (f-k) domain in which the propagation parameters are easily identified as spectral maxima. For the whole processing workflow, I used the SWAT matlab tool from Politechnico di Torino.

Once the spectral maxima are picked in the f-k domain, the resulting dispersion curves are given in the phase velocity-frequency (v-f) domain. The phase velocity v is calculated by:

$$v = \frac{2\pi f}{k} \tag{2-3}$$

where f is the frequency and k the corresponding wavenumber of the data points. The data quality can be improved by stacking. If this is not performed during the acquisition and hence data for each shot are available, stacking can be performed in the f-k domain (Socco et al. 2009).

Gaussian Windowing

When lateral variations might be present beneath the receiver spread, windowing in space domain can be applied prior to spectral analysis to obtain local dispersion curves and improve lateral resolution. Here I have adopted the method proposed by Bergamo et al. (2012). This technique extracts several dispersion curves along the survey line based on spatial windowing of several Gaussian Windows with different shapes. The width of the

Gaussian windows are based on the minimum resolvable wavenumber, wavenumber resolution and the desired lateral resolution. The extracted dispersion curve refers to the position of the corresponding window maximum, and representing the subsurface portion that is covered by the width of the Gaussian window.

2-2-3 Inversion

The last stage of the analysis involves inversion of the dispersion curves. For the usual inversion of the surface-wave analysis, the mechanical properties are inverted assuming a stack of linear elastic homogeneous layers. Where the properties of each layer are described by the following parameters: V_s, ρ, σ and layer thickness. For the inversion of these properties, only V_s and thickness are considered unknowns, using global search and deterministic algorithms (Socco et al. 2010). However, in this study I will perform the inversion by imposing a power-law trend to the $V_{p,s}$ and estimating the $\gamma_{p,s}$ and $\alpha_{p,s}$ given by formula 2-1. The ρ is assumed constant with depth based on the theoretical studies proving less sensitivity (Nazarian et al. 1983; Xia et al. 1999). Furthermore, Bergamo et al. (2013) shows that the estimated V_p if higher surface-wave modes are available also gives a reliable range of σ values.

For the inversion I will use the Monte Carlo multimodal inversion that allows all the experimental data points to be inverted at the same time, without the need to associate them to a specific mode (Maraschini and Foti 2010). The inversion code was implemented by Bergamo (2012). The misfit function is based on the absolute value of the Haskell-Thomson determinant, in which the zeros corresponds to the modal curves.

The theoretical dispersion curve required in the inversion process, is calculated using the forward modeling proposed by Haskell (1953) and Thomson (1950). This is done by creating a 1D medium of the layers whose thickness increases with depth according to a power-law.

2-3 Refraction travel-time inversion

Refraction method is mainly used in near-surface applications for bedrock and water-table mapping through compressional-wave (P-wave) velocity retrieval (Zhang and Toksöz 1998). Refraction occurs at the interface between two layers, characterized by a significant P-wave velocity (V_p) increase, shown in figure 2-3. This phenomenon is governed by the Snell's law:

$$\frac{\sin\theta_{ic}}{V_{p1}} = \frac{1}{V_{p2}} \tag{2-4}$$

where θ_{ic} is the critical angle for the commencement of refraction, and V_{p1} and V_{p2} are respectively the direct wave velocity (upper layer) and the refracted wave velocity (lower layer). The V_{p1} and V_{p2} are calculated from the travel-time diagrams after picking the first-arrival times of the seismograph. The slopes of the direct wave and refracted wave give respectively V_{p1} and V_{p2}. The depth of the water-table is calculated as:

$$H_0 = \frac{Vp_1 T_0}{2\cos_{\theta_{ic}}} \tag{2-5}$$

where T_0 is the intercept time shown in figure 2-3. In this study the first-arrival times are picked and inverted with the Sandmeier scientific software Reflexw.

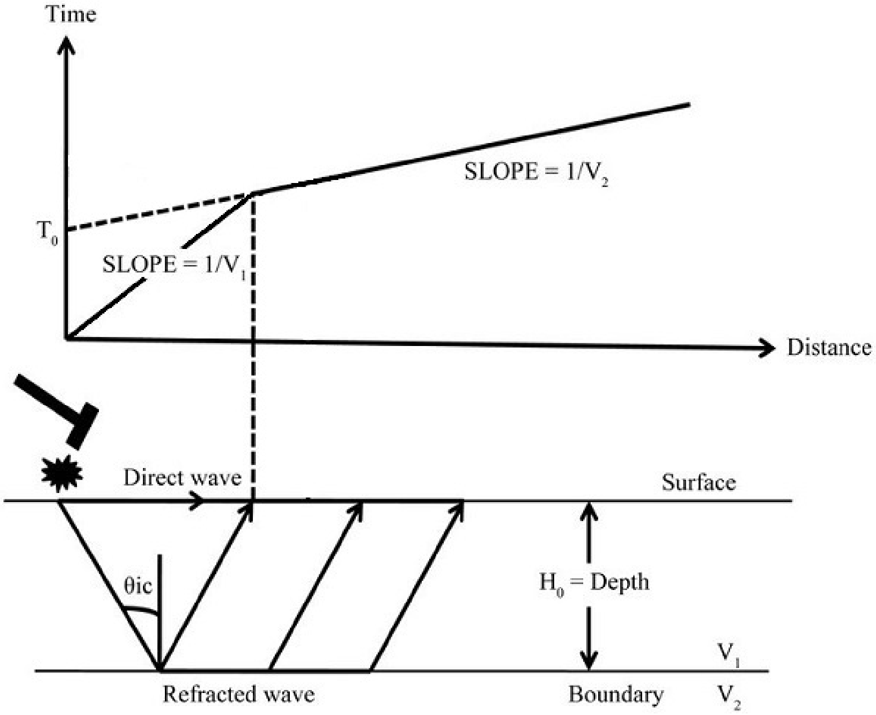

Figure 2-3: Schematic representation of the P-wave refraction method. Bottom: ray paths of direct and critically refracted waves. Top: Associated hodocrone in which the arrivals of direct waves and refracted waves lie on two lines whose slopes are inversely proportional to V_{p1} and V_{p2}, respectively..

Chapter 3

Field Experiment

In the previous chapter, I explained the theory of granular materials and the methods to perform characterization of loose granular materials. To investigate the properties of a loose granular material, I first acquired the seismic data over a sand dune in the Netherlands. In this chapter, I will describe the experimental site and the acquisition parameters followed by some raw data results.

3-1 Experimental site

In March 2015, I acquired field data at Wassenaar, located 52°09' N and 4°21' E in the Netherlands (behind the Fletcher Hotel Duinoord). The map of the Netherlands with the site location Wassenaar is denoted by the red star in figure 3-1. In figure 3-2, I show the google image of the experimental site with the illustration of the acquisition lines by the yellow line and red line, the Fletcher Hotel Duinoord is indicated by the yellow star. The experimental site, is located on a dune area that is owned by the water management company Dunea. The backyard of the Fletcher Hotel Duinoord was selected with permission of the Hotel and not from Dunea.

The experimental location is part of The Holland coast, which consists of sandy, multi-barred beaches and can be characterized as a wave dominated coast. Approximately 290 km of the coast consists of dunes and 60 km is protected by structures such as dikes and dams. The dunes, together with the beach and the shore face, offer a natural, sandy defense to the sea. According to the Actueel Hoogtebestand Nederland (AHN), the experimental area lies with an average height of 7.2 m above sea level ranging between 2.7 m and 13.2 m. The average maximum height of the water-table in the Netherlands coastal dune area is in the order of 5 m above sea level (Wong et al. 2007). The sediment of the Holland coast is well sorted and composed of fine to medium sand with a mean grain size between 250 and 350 μm (Sistermans and Nieuwenhuis 2004).

Figure 3-1: Map of the Netherlands with the site location, Wassenaar is located in the west of the Netherlands part of The Holland coast, denoted by the red star.

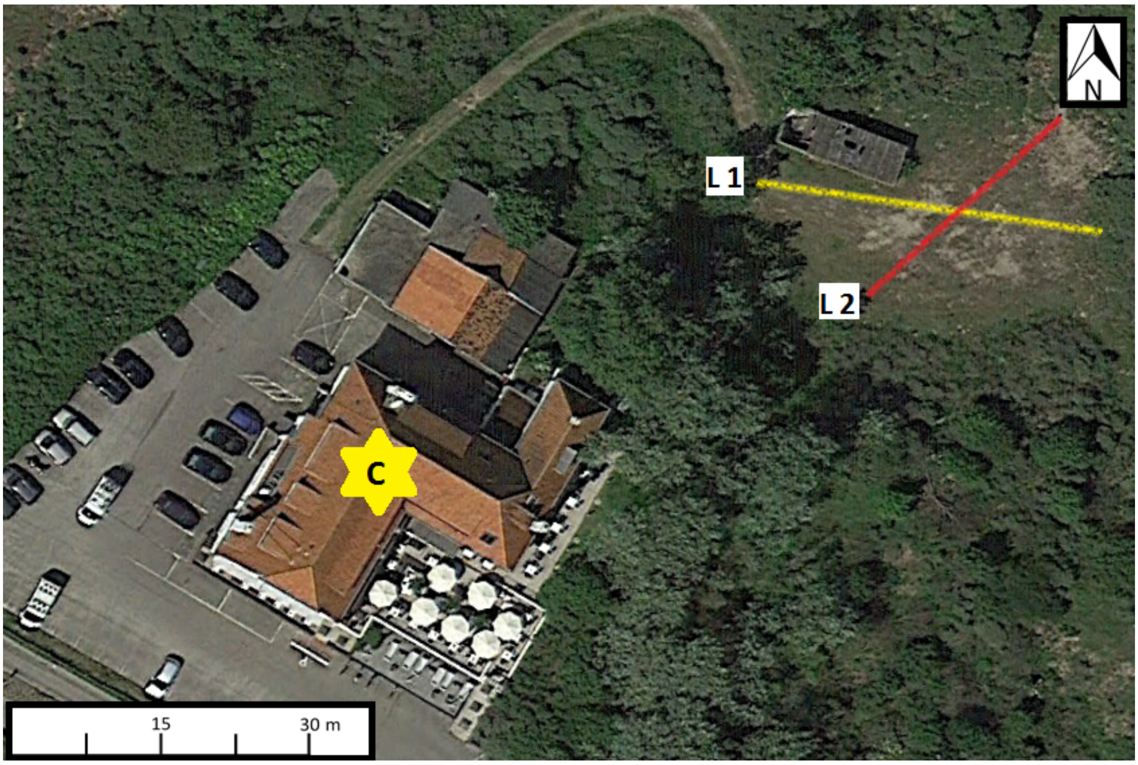

Figure 3-2: Google map of the experimental site located in Wassenaar, the Netherlands. The acquisiton lines 1 and 2 are respectively denoted by L1 (yellow) and L2(red). The Fletcher Hotel Duinoord is indicated by C, the yellow star.

3-2 Acquisition

Two acquisition lines were set up; line 1 and line 2 cross each other with an angle of 45°. Multichannel recording was performed with a maximum number of 120 geophones, 48 geophones on the seismograph and 3 geodes each with 24 channels. In figure 3-3, I show a picture of the field set up, line 1 and line 2 are denoted by the yellow line and red line. The white rectangles in figure 3-3 denotes the 3 geode of the set up.

Figure 3-3: Picture of the field set up, yellow line and red line denote respectively line 1 and line2. The geodes are denoted by the white rectangles.

The survey geometry is illustrated in figure 3-4 and the acquisition and recording parameters for the 2 acquisition lines are listed in Table 3-1. For a broad frequency band, I used impulsive sources varying in weight and vibroseis with different sweeps. The vibroseis is a high-frequency electromagnetic P-wave vibrator with a weight of 70 kg, and can generate any kind of sweep in the frequency range of 20 to 1500 Hz (Ghose et al. 1998). The natural frequency of the geophones are 10 Hz with vertical recording component and full wave recording components. The spread length and source-offset is limited because of the width of the experimental site. To avoid aliasing based on the Nyquist criterion, time sampling of 0.50 ms was selected. Some examples of recorded seismograms with the wavefield interpretation are shown in figure 3-5. The data are from acquisition along line 1 with receiver interval Δx=0.3 m using a sledgehammer, a vibroseis [sweep: 10Hz - 250Hz] and a weight drop source.

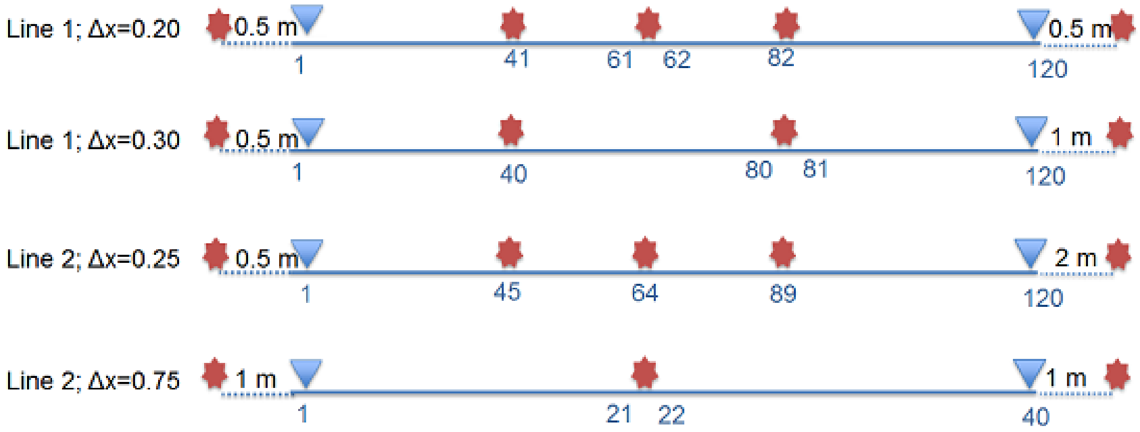

Figure 3-4: Line layout of acquisition line 1 and line 2 with the different Δx. The shots are illustrated by the red star symbol with the source-offset of the end shots marked, and the middle shot positions correspond to the receiver numbers below. The geophones are denoted by the blue triangle symbol at the end of the lines.

Table 3-1: Field acquisition and recording parameters for the 2 acquisition lines. For the vibroseis source the sweep are given in between the brackets.

	Line 1		Line 2	
Receiver type	vertical, 10 Hz	vertical, 10 Hz	vertical, 10 Hz	full wave, 10 Hz
Number of receivers	120	120	120	40
Receiver interval (Δx)	0.20 m	0.30 m	0.25 m	0.75 m
Profile length	23.80 m	35.70 m	29.75 m	29.25 m
Source offset	0.50 m	0.50 m, 1.00 m	0.50 m, 2.00 m	1.00 m
Time sampling interval (Δt)	0.50 ms	0.50 ms	0.50 ms	0.50 ms
Time window	500 ms	500 ms	500 ms	500 ms
Seismic source	Sledgehammer 5 kg	Sledgehammer 5 kg	Sledgehammer 5 kg	Sledgehammer 5 kg
	Weight drop 12 kg	Weight drop 12 kg	Weight drop 12 kg	Weight drop 12 kg
	Vibroseis [10,250]	Vibroseis [10,250]	Vibroseis [10,250]	Vibroseis [10,250]
	Vibroseis [10,450]	Vibroseis [10,450]	Vibroseis [10,450]	Vibroseis [10,450]
	Vibroseis [10,850]	Vibroseis [10,850]	Vibroseis [10,850]	Vibroseis [10,850]
	Vibroseis [50,850]	Vibroseis [50,850]	Vibroseis [50,850]	Vibroseis [50,850]

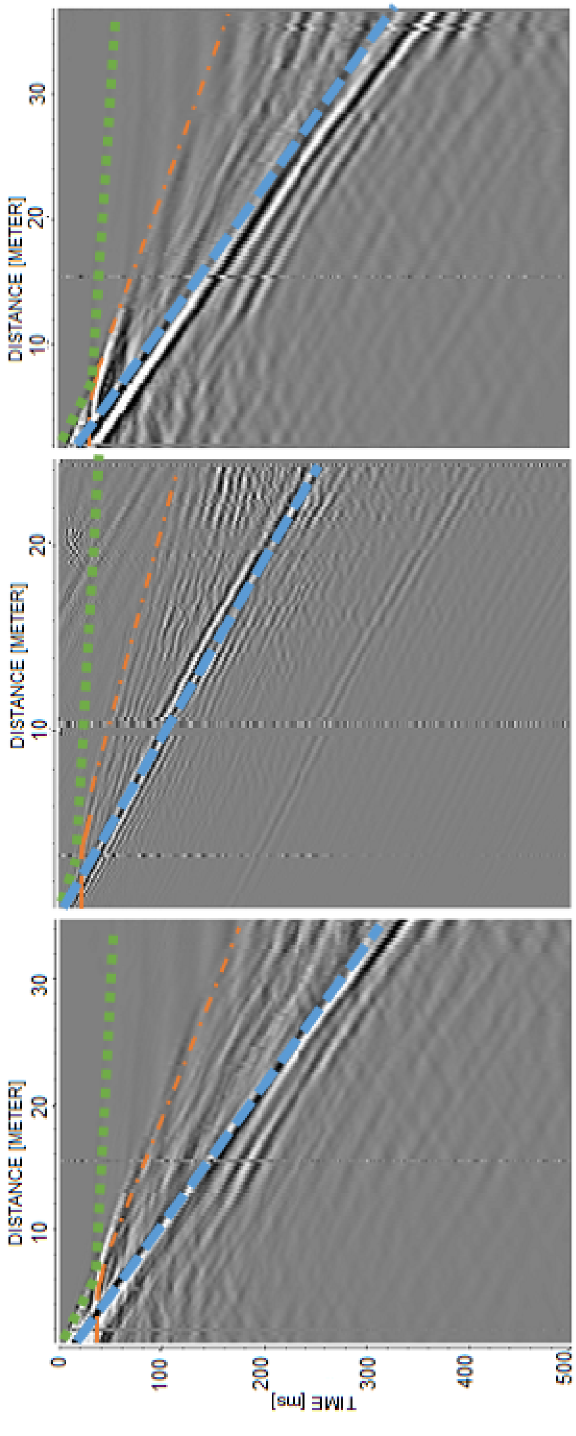

Figure 3-5: Recorded shotgathers; from left to right: hammer , vibroseis [sweep: 10Hz - 250Hz], weight drop. The refracted arrivals are given by the green line, the reflections by the orange line and the surface waves by the blue line. The source offset is 1 m, 120 traces per shot, Δx=0.30 m.

Chapter 4

Processing and Inversion results

After the seismic data was acquired, the processing and inversion on the retrieved data was performed. In this chapter, I will first show the results of the different analysis steps performed on the dispersion curves in the processing stage of the surface waves. Finally, I will show the results of the steps performed during the inversion stage.

4-1 Processing

Before analyzing the dispersion curves, processing of the raw seismic data is necessary to create the dispersion curves for the inversion explained in the method section 2-2. I have created several dispersion curves from the raw seismic data of the different shot positions along each line. Tables 4-1, 4-2 and 4-3 show the processing steps applied on the different shots along the acquisition line 1 and line 2. Each processing ID belongs to the shots (FFID) taken with the same source, shot position and window length. The range of the window length is selected based on the removal of the saturated traces at the beginning of the acquisition lines. Note that processing of the data from acquisition line 2 with Δx=0.75 m is not performed.

Now that the dispersion curves are created, I will start analyzing the dispersion curves on the frequency range to provide recommendations on the best practice in fieldwork. Afterwards, I will perform f-k domain stacking from different sources in order to improve the resolution. In the end, I investigate the dispersion curves on lateral variation using the Gaussian windowing technique explained in section 2-2. The workflow is outlined in figure 4-1.

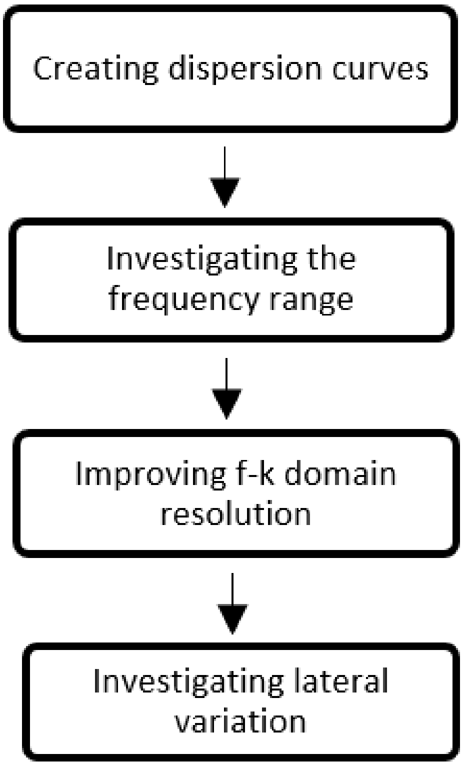

Figure 4-1: Process workflow for the processing stage on the raw seismic data.

Table 4-1: Table of the different processing steps applied on the shots (FFID) of line 1 with $\Delta x = 0.20$ m. For the vibroseis source the sweep are given in between the brackets. The shot position (Xs) and selected window range are given in meters. The used number of receivers are given by R.

	Line 1; $\Delta x = 0.20$ m					Processing steps				
Process ID	FFID	Source	Xs (m)	Window length (m)	R	Stacking	Muting	F-K	Picking	Gaussian
1	0057-0064	Hammer	0.2	[5.7 - 24.5]	95	x	x	x	x	x
2	0001-0008	Hammer	25	[0.7 - 18]	87	x	x	x	x	x
3	0065-0072	Weight drop	0.2	[8.5 - 24.5]	81	x	x	x	x	
4	0017-0024	Weight drop	25	[0.7 - 18]	87	x	x	x	x	
5	0129-0136	Sweep[10Hz - 250Hz]	0.2	[3.8 - 24.5]	104	x	x	x	x	
6	0169-0176	Sweep[10Hz - 250Hz]	12.6							x
7	0089-0096	Sweep[10Hz - 250Hz]	25	[0.7 - 22.9]	111	x	x	x	x	x
8	0121-0128	Sweep[10Hz - 450Hz]	0.2	[3.1 - 24.5]	108	x	x	x	x	
9	0081-0088	Sweep[10Hz - 450Hz]	25	[0.7 - 21.55]	105	x	x	x	x	
10	0113-0120	Sweep[10Hz - 850Hz]	0.2	[4.3 - 24.5]	101	x	x	x	x	
11	0073-0080	Sweep[10Hz - 850Hz]	25	[0.7 - 21.6]	105	x	x	x	x	
12	0137-0144	Sweep[50Hz - 850Hz]	0.2	[3.9 - 24.5]	103	x	x	x	x	
13	0097-0104	Sweep[50Hz - 850Hz]	25	[0.7 - 21.6]	105	x	x	x	x	

Table 4-2: Table of the different processing steps applied on the shots (FFID) of line 1 with $\Delta x = 0.30$ m. For the vibroseis source the sweep are given in between the brackets. The shot position (Xs) and selected window range are given in meters. The used number of receivers are given by R.

	Line 1; $\Delta x = 0.30$ m									
Process ID	FFID	Source	Xs (m)	Window length (m)	R	Stacking	Muting	F-K	Picking	Gaussian
14	0386-0393	Hammer	0.2	[7.8 - 36.4]	96	x	x	x	x	x
15	0386-0393	Hammer	0.2	[7.8 - 32.8]	84	x	x	x	x	
16	0386-0393	Hammer	0.2	[7.8 - 25.8]	60	x	x	x	x	
17	0386-0393	Hammer	0.2	[18 - 36.4]	62	x	x	x	x	
18	0370-0377	Hammer	25	[0.7 - 18]	58	x	x	x	x	x
19	0363-0369	Hammer	37.4	[0.7 - 29.45]	96	x	x	x	x	x
20	0363-0369	Hammer	37.4	[0.7 - 18]	58	x	x	x	x	
21	0363-0369	Hammer	37.4	[4.6 - 29.45]	83	x	x	x	x	
22	0363-0369	Hammer	37.4	[11.5 - 29.45]	60	x	x	x	x	
23	0395-0402	Weight drop	0.2	[8.45 - 36.4]	94	x	x	x	x	
24	0411-0418	Weight drop	25	[0.7 - 16]	52	x	x	x	x	
25	0419-0426	Weight drop	37.4	[0.7 - 27.2]	89	x	x	x	x	
26	0250-0257	Sweep[10Hz - 250Hz]	0.2	[3.5 - 36.4]	110	x	x	x	x	x
27	0290-0297	Sweep[10Hz - 250Hz]	25	[0.7 - 22.5]	73	x	x	x	x	
28	0330-0337	Sweep[10Hz - 250Hz]	37.4	[0.7 - 35]	115	x	x	x	x	x
29	0330-0337	Sweep[10Hz - 250Hz]	37.4	[7 - 35]	94	x	x	x	x	
30	0242-0249	Sweep[10Hz - 450Hz]	0.2	[2.8 - 36.4]	112	x	x	x	x	
31	0322-0329	Sweep[10Hz - 450Hz]	37.4	[0.7 - 34.6]	113	x	x	x	x	
32	0233-0241	Sweep[10Hz - 850Hz]	0.2	[3.1 - 36.4]	111	x	x	x	x	
33	0314-0321	Sweep[10Hz - 850Hz]	37.4	[0.7 - 34.6]	113	x	x	x	x	
34	0258-0265	Sweep[50Hz - 850Hz]	0.2	[3.4 - 36.4]	110	x	x	x	x	
35	0338-0345	Sweep[50Hz - 850Hz]	37.4	[0.7 - 34.3]	112	x	x	x	x	

Table 4-3: Table of the different processing steps applied on the shots (FFID) of line 2 with $\Delta x = 0.25$ m. For the vibroseis source the sweep are given in between the brackets. The shot position (Xs) and selected window range are given in meters. The used number of receivers are given by R.

	Line 2; $\Delta x = 0.25$ m					Processing steps				
Process ID	FFID	Source	Xs (m)	Window length (m)	R	Stacking	Muting	F-K	Picking	Gaussian
36	0846-0853	Hammer	0	[6.5 - 30.25]	95	x	x	x	x	
37	0863-0870	Hammer	32.25	[0.5 - 24]	94	x	x	x	x	
38	0887-0894	Weight drop	0	[7.4 - 30.25]	92	x	x	x	x	
39	0871-0878	Weight drop	32.25	[0.5 - 18.8]	74	x	x	x	x	
40	0798-0805	Sweep[10Hz - 250Hz]	0	[3.8 - 30.25]	106	x	x	x	x	
41	0629-0636	Sweep[10Hz - 250Hz]	20.25	[0.5 - 16.2]	63	x	x	x	x	
42	0541-0548	Sweep[10Hz - 250Hz]	32.25	[0.5 - 29.1]	114	x	x	x	x	

4-1-1 Frequency range investigation

To provide recommendations for the best practice in field work, I will investigate the frequency range of the processed dispersion curves. I will compare the f-k domain and the corresponding dispersion curves taken from the sledgehammer, vibroseis [sweep: 10Hz - 250Hz] and weight drop. In figure 4-2, I first show the f-k domain of the data in line 1 with $\Delta x = 0.20$ m (Top) and $\Delta x = 0.30$ m (Bottom). The high energy is in the red color and the picked energy maxima for the dispersion curves is indicated by the white stars (line) on top of the red color. The resulting dispersion curves are plotted in figure 4-3 and 4-4.

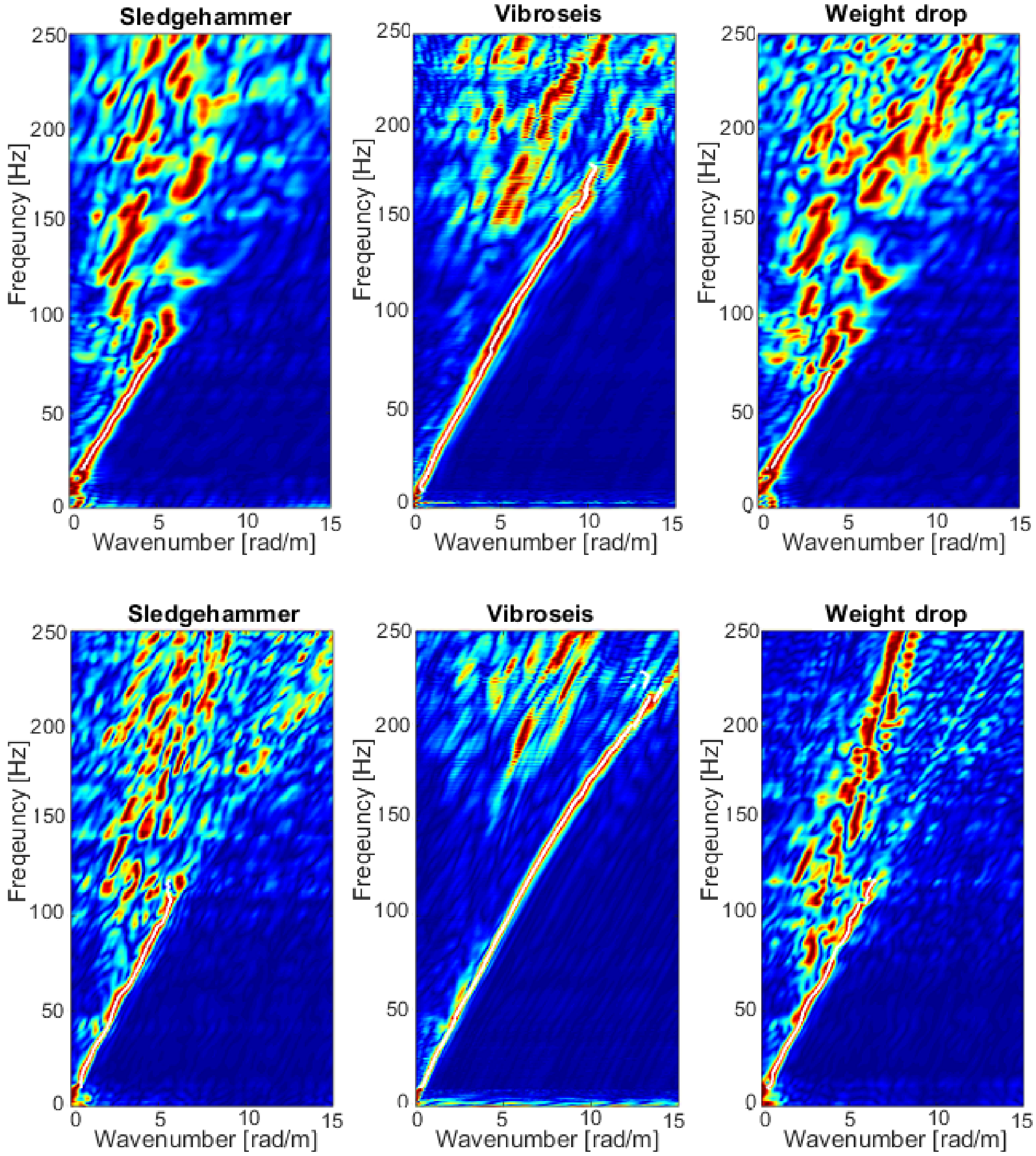

Figure 4-2: F-k domain from the sledgehammer, vibroseis [sweep: 10Hz - 250Hz] and weight drop data in line 1. Top: $\Delta x = 0.20$ m and 0.5 m source offset. From left to right the data corresponds to the processing ID 2, 7 and 4 (Table 4-1). Bottom: $\Delta x = 0.30$ m and 1.0 m source offset. From left to right the data corresponds to the processing ID 19, 28 and 25 (Table 4-2).

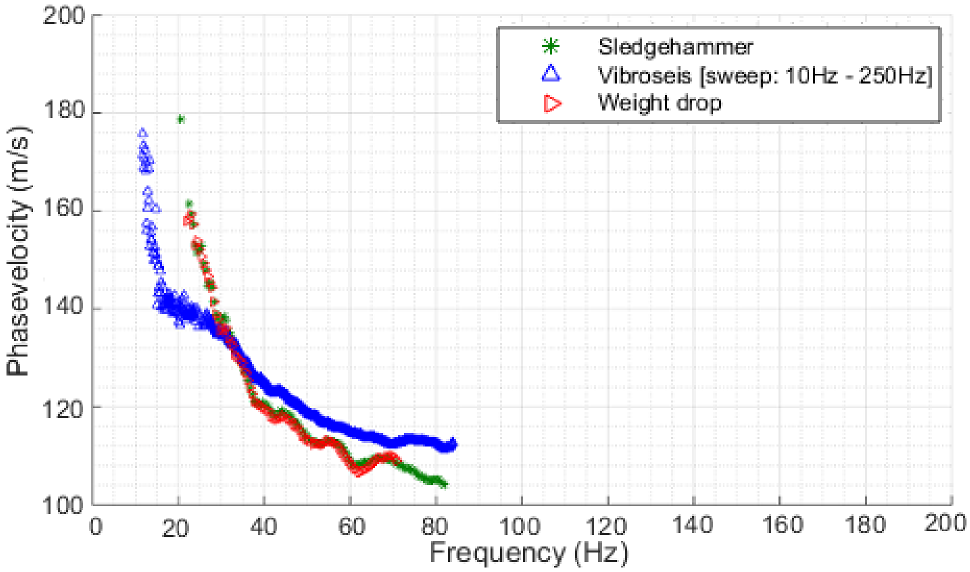

Figure 4-3: The resulting dispersion curves of line 1 with $\Delta x = 0.20$ m and 0.5 m source offset from the picked energy maxima in the f-k domain shown in the top of figure 4-2. The dispersion curves of the sledgehammer, vibroseis [sweep: 10Hz - 250Hz], and weight drop are denoted by the green, red and blue curve.

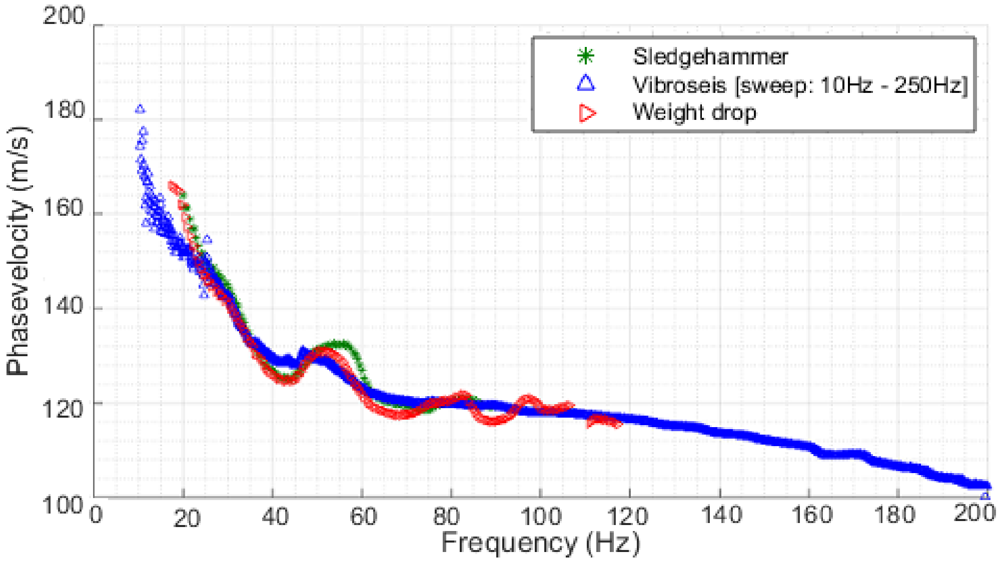

Figure 4-4: The resulting dispersion curves of line 1 with $\Delta x = 0.30$ m and 1.0 m source offset from the picked energy maxima in the f-k domain shown in the bottom of figure 4-2. The dispersion curves of the sledgehammer, vibroseis [sweep: 10Hz - 250Hz], and weight drop are denoted by the green, red and blue curve.

From analysis of the f-k domain it is clearly seen that the vibroseis [sweep: 10Hz - 250Hz] in figure 4-2 on acquisition line 1 with $\Delta x = 0.30$ m has the broadest continuous frequency range. The sledgehammer and weight drop data are nearly continuous in the same frequency range in the f-k domain, although in line 1 with $\Delta x = 0.30$ m the continuous energy maxima has a slightly broader frequency range that can be clearly seen from the dispersion curve retrieved from the weight drop in figure 4-4. In addition, line 1 with $\Delta x = 0.30$ m has a longer spread length than line 1, thus it should give a better spectral resolution and should make higher modes easy to distinguish (Foti et al. 2014). Although there are no higher surface-wave modes detected.

Next, I analyze the corresponding dispersion curves from the sledgehammer, vibroseis and weight drop shown in figures 4-3 and 4-4. When comparing the dispersion curves, it becomes clear that the curves from line 1 with $\Delta x = 0.30$ m cover a broader frequency range. Especially the vibroseis data that covers a higher frequency range than the sledge hammer and weight drop due to the advantage of the continuous sweep that cover the whole frequency band 10Hz to 250Hz in a single signal (Foti et al. 2014). In addition, I will compare the data of line 2 with line 1 for further investigation on the frequency range. The picked energy maxima of line 2 with $\Delta x = 0.25$ m from the sledgehammer, vibroseis [sweep: 10Hz - 250Hz] and weight drop is displayed in figure 4-5. The resulting dispersion curves are plotted in figure 4-6.

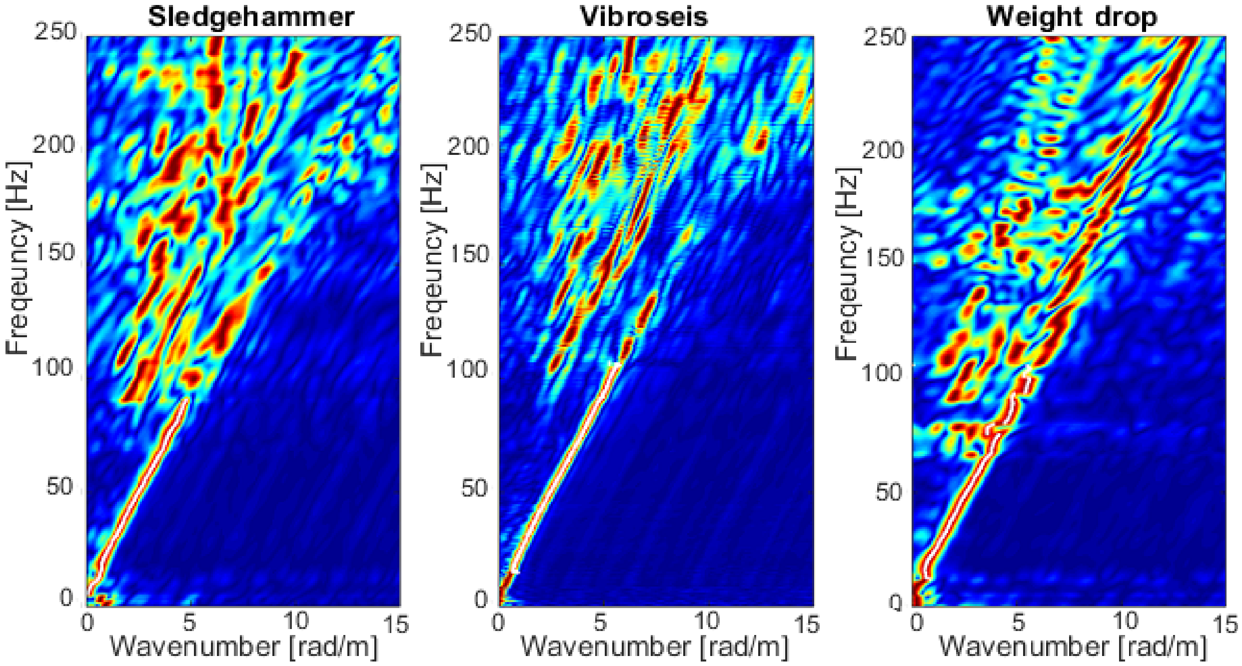

Figure 4-5: F-k domain from the sledgehammer, vibroseis [sweep: 10Hz - 250Hz] and weight drop data in line 2 with $\Delta x = 0.25$ m and 2.0 m source offset. From left to right the data corresponds to the processing ID 37, 42 and 39 (Table 4-3) .

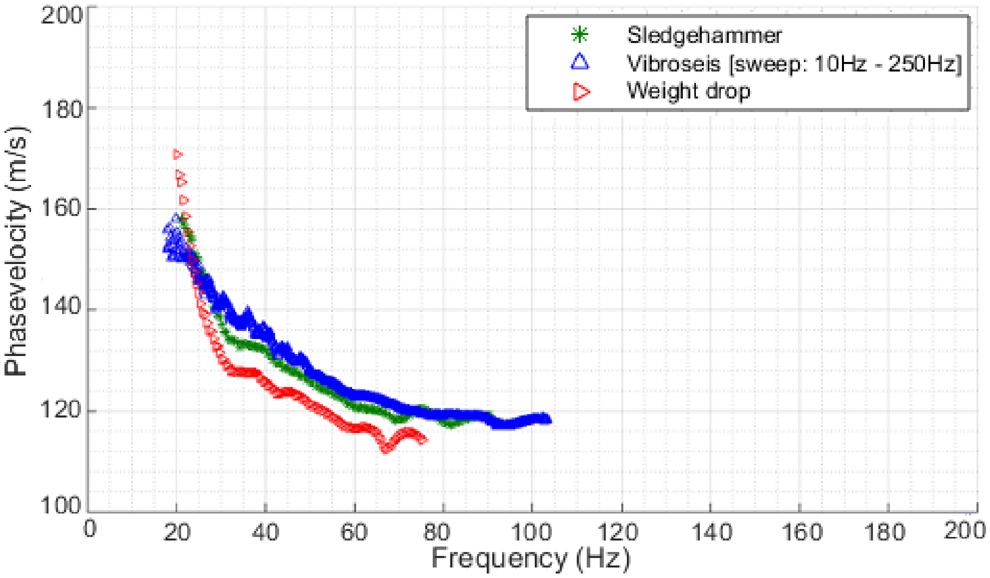

Figure 4-6: The resulting dispersion curves of line 2 with Δx = 0.25 m and 2.0 m source offset from the picked energy maxima in the f-k domain shown in the bottom of figure 4-5. The dispersion curves of the sledgehammer, vibroseis [sweep: 10Hz - 250Hz], and weight drop are denoted by the green, red and blue curve. .

Comparing the f-k domain results of line 2 (Fig. 4-5) with those of line 1 (Fig. 4-2), the data of line 2 is less continuous in the higher frequency range. This behavior can be clearly seen in the dispersion curve of the vibroseis source in figure 4-6. In the results of the f-k domain there is only one mode picked, the fundamental mode. Therefore I will perform in the next section stacking of the data in the f-k domain in an attempt to receive higher order surface modes.

4-1-2 F-k domain stacking

I will stack f-k spectra from different sources to increase the resolution for resolving the detection of higher surface-wave modes. I will stack the vibroseis data of acquisition line 1, with the following sweeps; [10Hz - 250Hz], [10Hz - 450Hz], [10Hz - 850Hz] and [50Hz - 850Hz] in the f-k domain. This data was selected based on the results of the previous section on frequency investigation that shows for the vibroseis data along line 1 with $\Delta x =$ 0.30 m the broadest and most continuous frequency range. The results are shown in figure 4-7, with the picked energy maxima on the left and the right plot illustrating the resulting dispersion curve in the v-f domain. Yet, the results do not show any improvement in the number of modes, which states that they are not excited in this experiment. Although the results do not show any improvement in the number of modes, the resulting dispersion curve will be used for further investigation in the Monte Carlo inversion process.

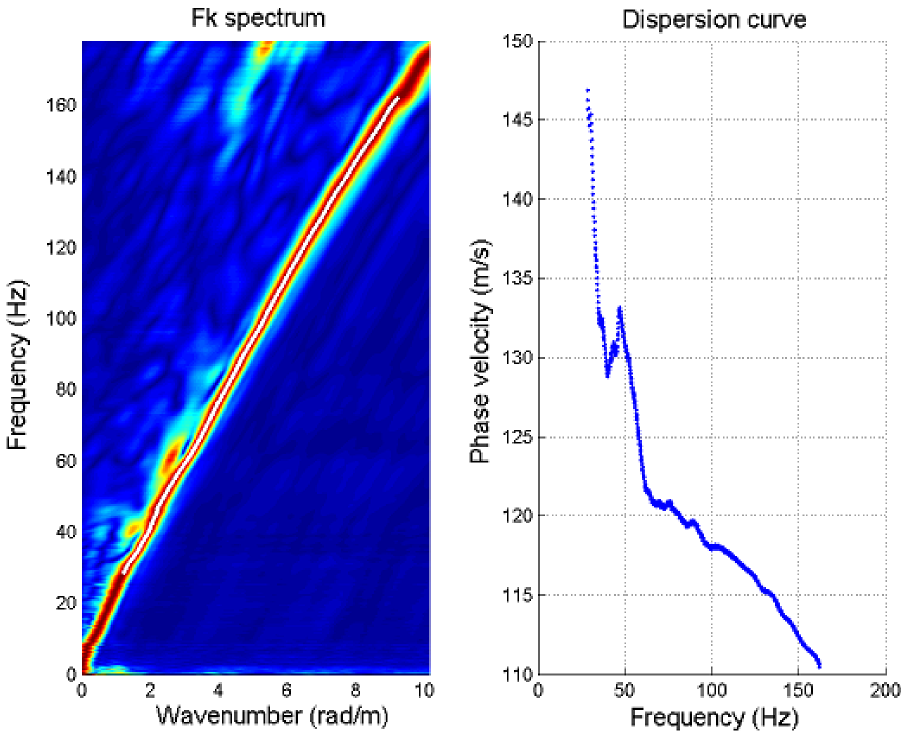

Figure 4-7: Left: Picked energy maxima of the vibroseis data along accquisition line 1 with Δx = 0.30 m after stacking the following sweeps; [10Hz - 250Hz], [10Hz - 450Hz], [10Hz - 850Hz] and [50Hz - 850Hz]. Right: The resulting dispersion curve plotted as phase velocity against frequency, without higher order of surface modes.

4-1-3 Lateral variation investigation

To investigate the presence of lateral variation along the acquisition line 1, I will apply the Gaussian windowing technique. Before applying the Gaussian windowing technique, I will analyze the dispersion curves from the vibroseis data taken at three different shot positions along line 1 with $\Delta x = 0.30$ m and line 2. The different shot positions from the vibroseis data of line 1 and line 2 are plotted respectively in figures 4-8 and 4-9. It is clearly seen that in figure 4-8 the middle shot Xs=25 m shows a strong deviation from the begin Xs=0.2 m and end shots Xs=37.40 m. The phase velocity starts from f=30 Hz shifting towards a lower velocity region. The results in figure 4-9 show the same deviated behavior as in figure 4-8 starting from f=40 Hz towards the lower velocity region. This behavior is further investigated with the Gaussian windowing technique.

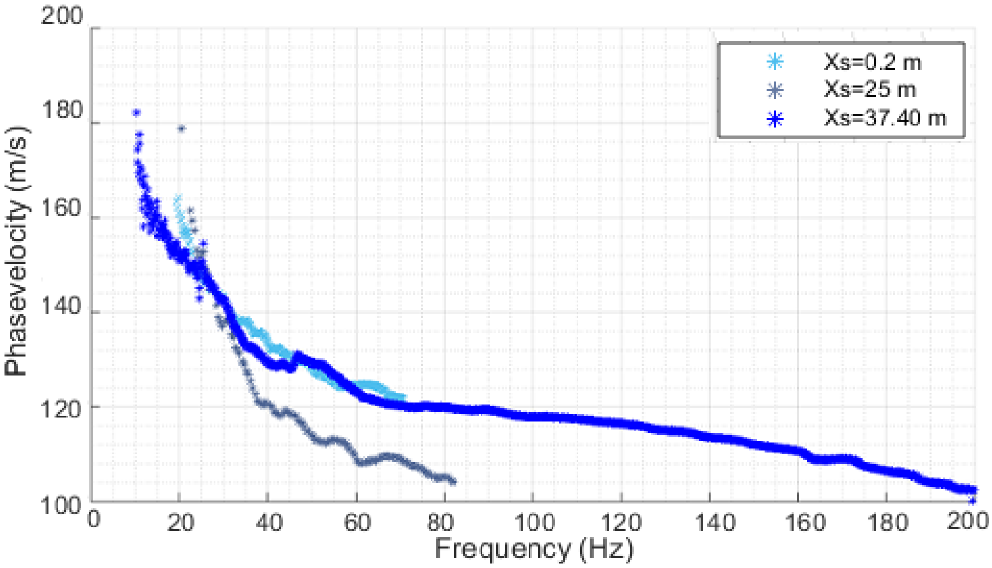

Figure 4-8: The dispersion curves of the vibroseis [sweep: 10Hz - 250Hz] data along acquisition line 1 with $\Delta x = 0.30$ m for 3 different shots: Xs=0.2 m, Xs=25 m, Xs=37.40 m with respectively the processing ID 26,27 and 28 in Table 4-2.

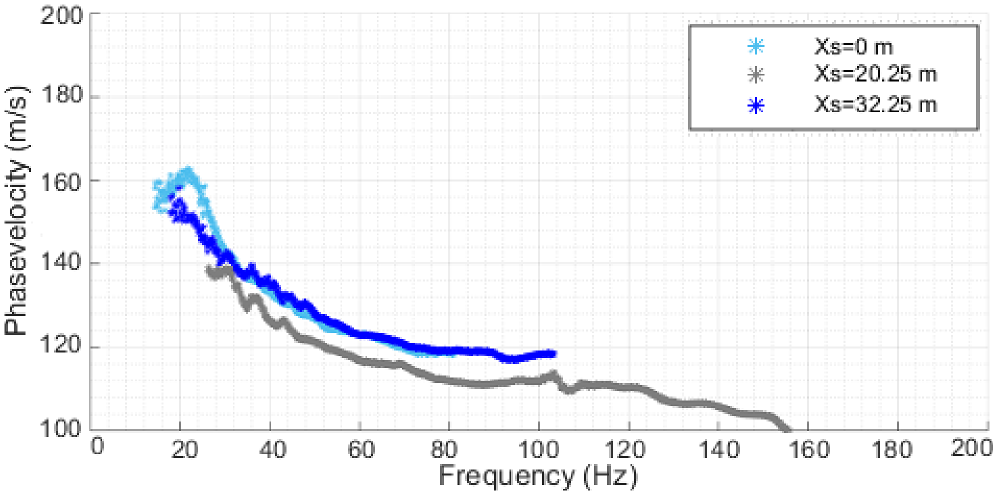

Figure 4-9: The dispersion curves of the vibroseis [sweep: 10Hz - 250Hz] data along acquisition line 2 for 3 different shots: Xs=0 m, Xs=20.25 m, Xs=32.25 m with respectively the processing ID 40,41 and 42 in Table 4-3.

I apply the Gaussian windowing technique that investigates the presence of lateral variation on the vibroseis data of acquisition line 1 shown in figure 4-8. Before applying the Gaussian windowing technique, I stack all the individual shots from each shot position. I transform this stacked data to the f-k domain. In the f-k domain I select the minimum resolvable wave number resolution that calculates the width of the Gaussian windows. This width of the Gaussian window relates to the lateral resolution of the dispersion curve. The results are shown in figure 4-10. Each dispersion curve has a lateral resolution of 12 m along the line. The three-colored dispersion curves are referring to the position of the receiver number, given in the legend. The curve at receiver number 41, referring to position $\Delta x \times 41 = 12.3$ m, deviates from f= 20Hz towards a lower velocity region. This deviated behavior was also detected in figures 4-8 and 4-9. Thus from the results of the Gaussian windowing technique, it can be stated that their is a lateral variation along the line.

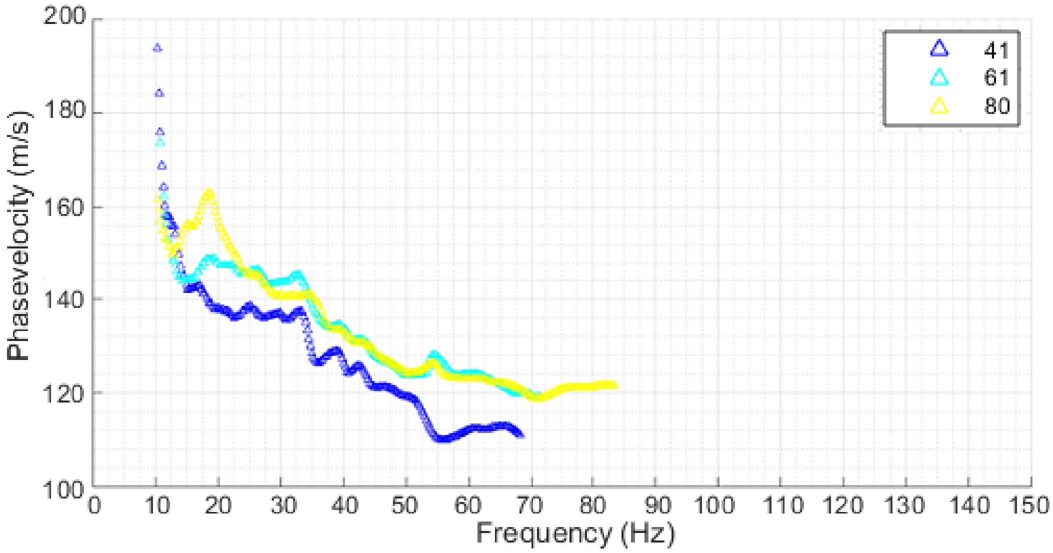

Figure 4-10: The dispersion curves retrieved by applying the Gaussian windowing technique. The dark blue, light blue and yellow colored dispersion curves refers to the position of receiver number 41,61 and 80 respectively. In geometric distances; 13 m, 19 m and 24.7 m respectively.

Although this does not yet give a clear identification on the range along the acquisition line that falls into the lower velocity region. Therefore further investigation was made on the data from the hammer with $\Delta x = 0.20$ m and $\Delta x = 0.30$ m. In figure 4-11 the dispersion curves corresponding to different window lengths and different shot positions along line 1 are shown. From the results it can be stated that the dispersion curves calculated for a window length starting at 7 m falls into the higher velocity region, although Xs=37.40 m [range= 0.7m - 29.45m] falls as well into the higher velocity region. Due to the large window lengths, starting from 0.7 m like the shots at 25 m and 25.20 m falling both into the higher velocity region, it clears out the lower velocity region.

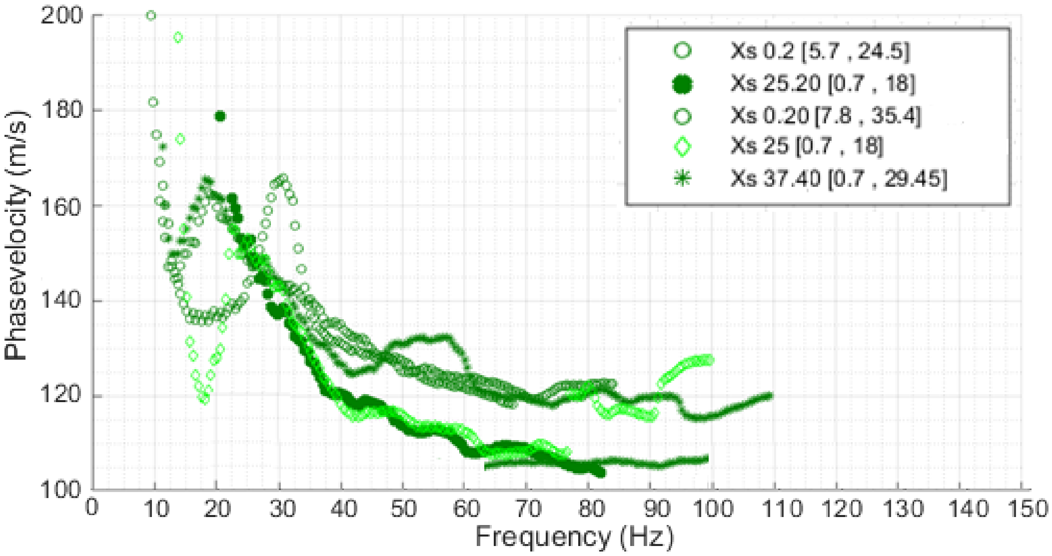

Figure 4-11: Dispersion curves for different shot positions of the hammer data, along acquisition line 1 with $\Delta x = 0.20$ m and $\Delta x = 0.30$ m . The dispersion curves denoted in the legend corresponds respectively to the processing ID 1, 2, 14, 18 and 19 in Tables 4-1 and 4-2.

4-2 Inversion

In this section the near-surface shear wave velocity profiles will be inverted by imposing a power-law trend to the velocity and estimating the power-law coefficients γ_s and α_s, explained in section 2-2-3. The results of the dispersion curves do not show any higher surface-wave modes, thus will the inversion be applied only for retrieving shear-wave velocity V_s profiles. Before showing the results of the Monte Carlo inversion on the dispersion curves, the refraction travel-time inversion results are presented for the estimation of the water-table position. The process workflow for the inversion is outlined in figure 4-12.

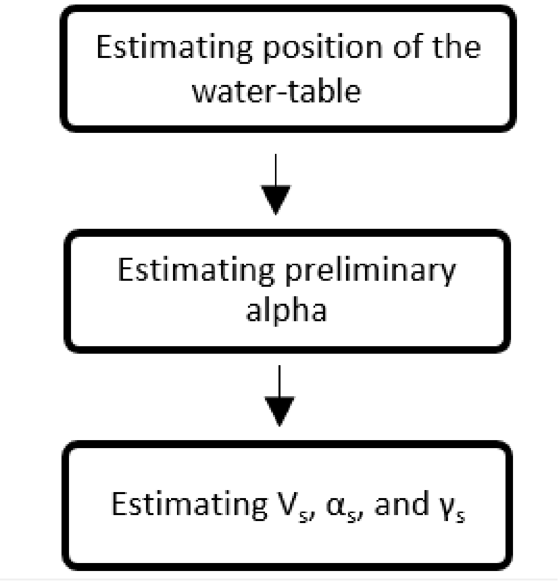

Figure 4-12: Process workflow for the inversion applied on the dispersion curves.

4-2-1 Position of the water-table

To investigate the position of the water-table, I will invert the travel-times of the refracted arrivals. The position of the water-table is important for including the affect on the inversion results of the V_s, γ_s and α_s. I picked the first arrivals of the hammer data along acquisition line 1 with $\Delta x = 0.30$ m. In figure 4-13 the experimental travel-time versus offset curve is presented at each shot position. From the curve a non-linear behavior is observed in the increase of travel-time with source-receiver distance. Figure 4-14 shows the plot of the picked travel-times in different colors. The picks corresponding to the first layers are denoted with the green color and the second layer by the blue color. The black colored picks are not used for the travel-time inversion due to their irregular behavior.

The derived P-wave velocity from the inversion performed on the travel-times of the first layer and second layer is displayed in Table 4-4. In figure 4-15 the inverted depth of layer 2 is illustrated. This depth gives an estimation of the water-table position starting at ∼ 3 m at the end of the line to greater depths towards the beginning of the line.

Table 4-4: Results of the travel-time inversion. The average depth range of the layers are given in between the brackets.

	Layer 1	Layer 2
$V_p(m/s)$	303.53	1421.90
Depth (m)	[0 - 3]	[3 , -]

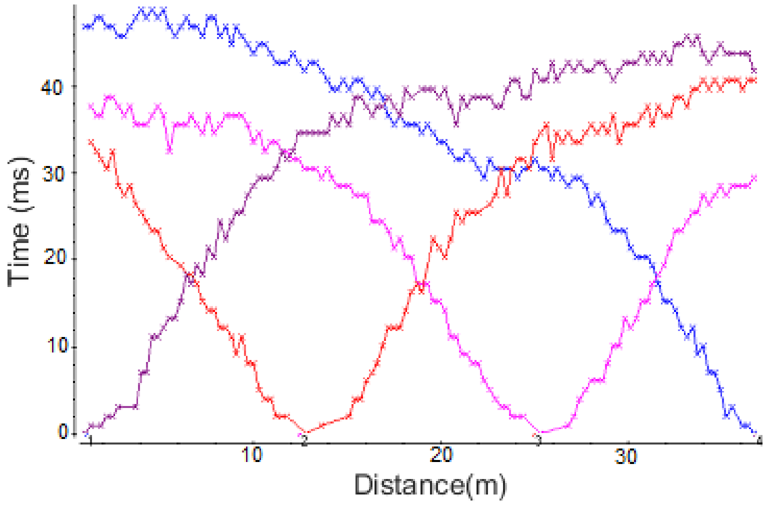

Figure 4-13: Traveltime versus offset plot of picked first-arrival, displayed with different colors depending on the source position. The blue, pink, red and purple traveltime diagram are respectively belonging to the following shot position in meters; 0.2, 12.50, 25 and 37.40.

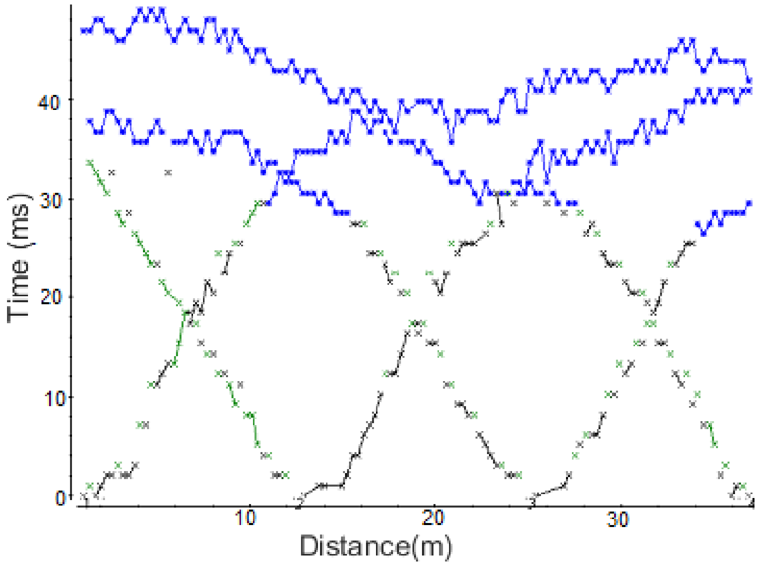

Figure 4-14: Selected data points of the picked first-arrivals belonging to the different layers. The green and blue stars belong to respectively the first layer and second layer. The black stars are not selected due to their irregular behavior.

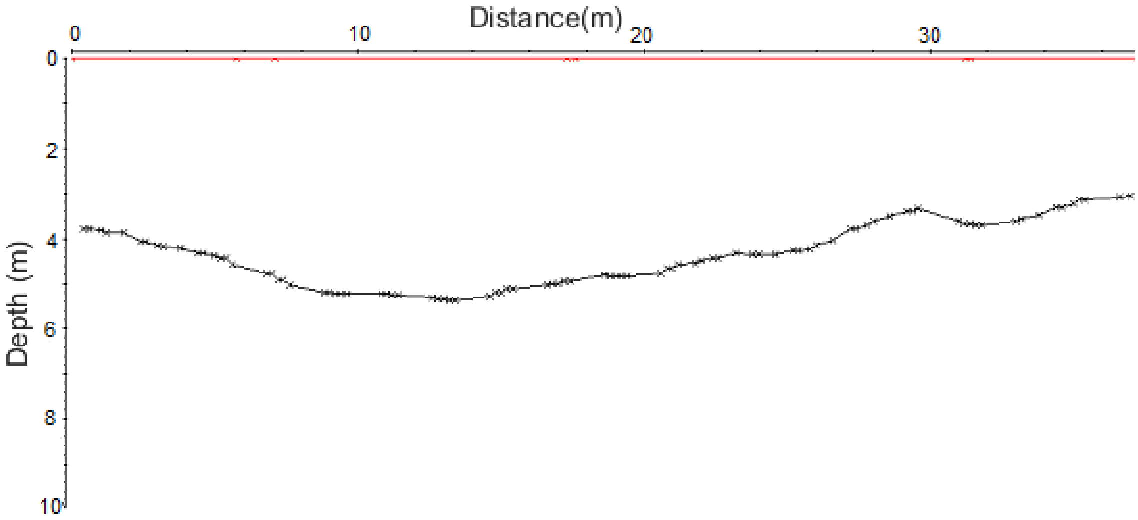

Figure 4-15: Depth profile of the refractor from first-arrival inversion over the spreadlength of acquisition line 2. The inverted depth corresponds to the water-table position, starting at ∼ 3 m at the end of the line to greater depths towards the beginning of the line.

4-2-2 Estimation of a preliminary value of alpha

Before I invert for the V_s, γ_s and α_s, I need to preliminary estimate the α_s for the input values of the Monte Carlo inversion. I estimated the preliminary alpha (α_s) by plotting the dispersion curves in linear and logarithmic scale. From the logarithmic plot the data points are selected that follows a linear behavior. These selected data points follows a power-law trend in linear scale. For the preliminary alpha estimation I selected the dispersion curves with the broadest and most continuous frequency band along each acquisition line. For line 1, I also selected the dispersion curve created by stacking f-k spectra of the vibroseis with different sweep, shown in section 4-1-2.

In Table 4-5 the results are given for the dispersion curves of each line with a broad and continuous frequency band. The data points of the vibroseis stack starts to follow from 2 m a different power-law trend, which is in logarithmic scale also a linear line but not coincident to the first part. In Table 4-5 this is called the second portion. Figures 4-16, 4-17 and 4-18 show the results of the selected data points of respectively the vibroseis stack, second portion and weight drop line 2. These will be further used for the inversion of the V_s profiles of each line in the next section, due to their value close to the literature and theoretical values given for α_s in section 2-1.

In addition, the dispersion curve of the vibroseis stack line 1 correspond to a window range of 0.7 m until 34.3 m, which includes the part that gives a lower velocity trend investigated in section 4-1-3. Due to the window range that covers the lateral variation along the line, the alpha value is not reliable for inversion. Furthermore, the dispersion curve of the weight drop data of line 2 over a distance of 0.25 m until 18.6 m covers the lower phase-velocity region that is also identified along acquisition line 1.

Table 4-5: Results of the preliminary alpha estimation for line 1 and line 2. The sources of the corresponding dispersion curves are denoted by VS and WD respectively vibroseis and weight drop. The range of the window lengths are given in between the brackets.

	Alpha (α)
VS 10450 Line 1 [7.0 , 24.5]	0.4619 ± 0.0239
VS stack Line 1 [0.7 - 34.3]	0.2242 ± 0.0062
VS stack Line 1 [7.0 - 34.3]	0.1692 ± 0.0015
Second Portion [7.0 - 34.3]	0.2391 ± 0.0051
VS 10250 Line 2 [0.5 - 16.2]	0.3939 ± 0.0210
VS 10250 Line 2 [0.5 - 29.1]	0.0264 ± 0.0037
WD Line 2 [0.5 - 18.8]	0.1963 ± 0.0080

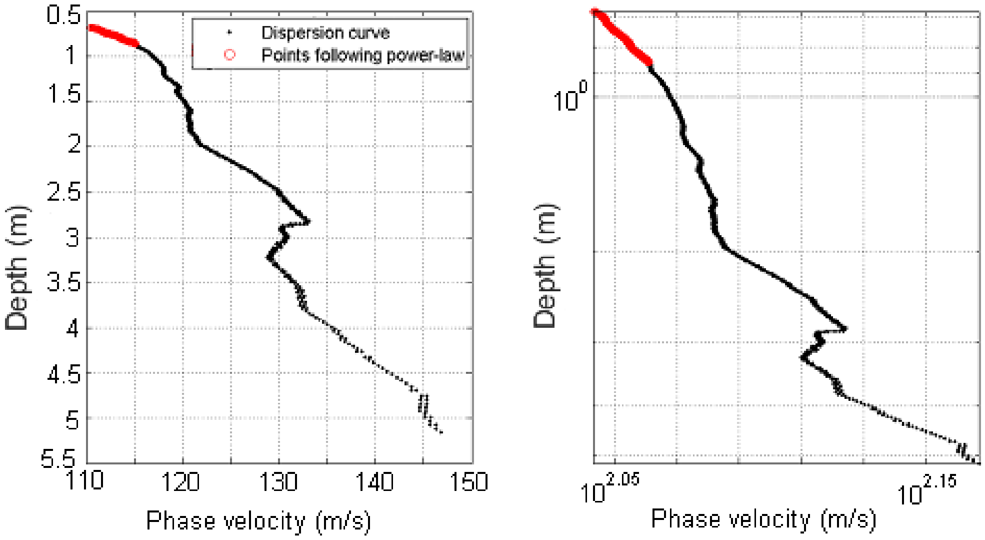

Figure 4-16: Selected data points in red for the preliminary estimation of alpha for the vibroseis stack of line 1. Left: Dispersion curve plot in linear scale. Right: Dispersion curve plot in logarithmic scale. The selected data points in logarithmic scale follows a power-law trend in linear scale.

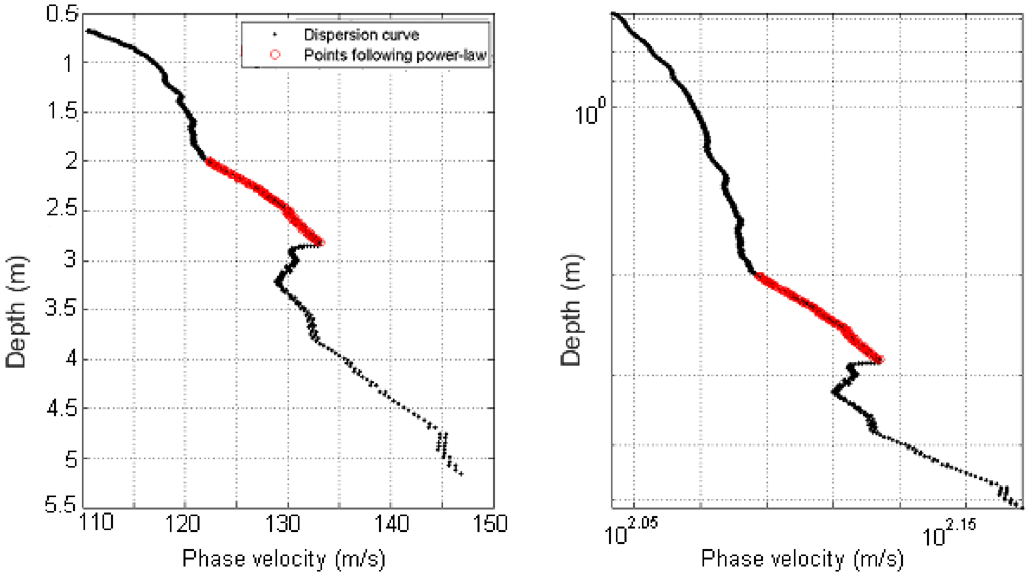

Figure 4-17: Selected data points in red for the preliminary estimation of alpha for the second portion of the vibroseis stack of line 1. Left: Dispersion curve plot in linear scale. Right: Dispersion curve plot in logarithmic scale. The selected data points in logarithmic scale follows a power-law trend in linear scale.

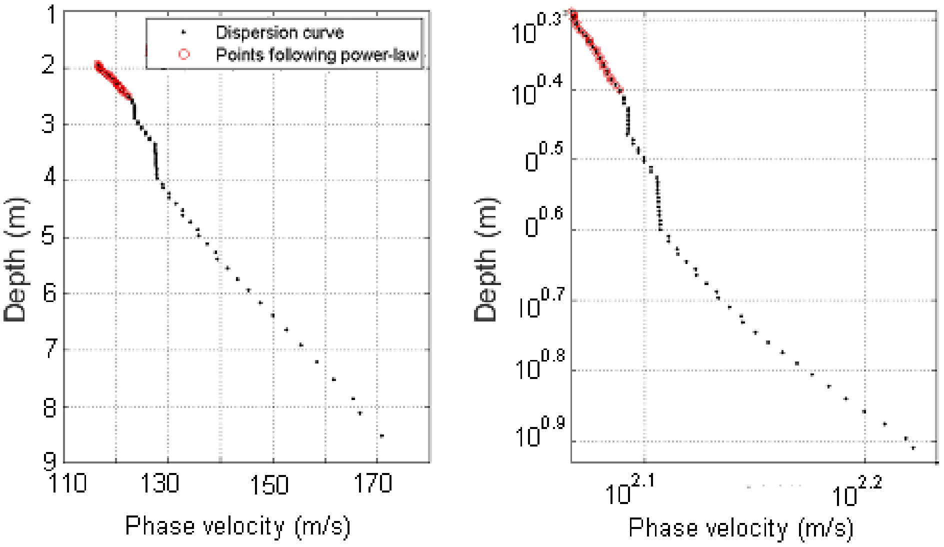

Figure 4-18: Selected data points in red for the preliminary estimation of alpha for the weight drop line 2 [range= 0.25m - 18.6m]. Left: Dispersion curve plot in linear scale. Right: Dispersion curve plot in logarithmic scale. The selected data points in logarithmic scale follows a power-law trend in linear scale.

4-2-3 Shear-wave velocity profile

In this section I will invert the shear-wave velocity profile V_s assuming a power-law trend to the velocity profile and estimating the power-law coefficients, γ_s and α_s. The V_s power-law trend that will be used for the Monte Carlo inversion is given by formula 2-1 in section 2. The data points that will be used as input for each of the V_s profiles are the selected data points for the preliminary alpha estimation in the previous section (4-2-2). For the estimation of the V_s along line 1, I will use the vibroseis stack data created from the different sweeps in section 4-1-2. For the inversion of the second layer, I will introduce a power-law that is influenced by the overburden of the first layer and with different power-law coefficients. For line 2, I will use the weight drop data that corresponds to the processing ID 39 in Table 4-3. I will first show the results of the data points belonging to the first layer of the vibroseis stack and weight drop before introducing the power-law for the second layer along line 1.

The input parameters for the Monte Carlo inversion of each line are given in Table 4-6. The α_s is from the preliminary estimation in section 4-2-2, and the range of gamma γ_s is between 4.5 and 25 based on the synthetic study of Bergamo et al. (2013) and a value of 19.31 for the natural dry sand of Galveston Beach (Texas) following Zimmer et al. (2006). For the density I will use a value of 1560 kg/m^3 based on the synthetic study by Bergamo et al. (2013) thatvuses a constant ρ of 1536 kg/m^3 for the Galveston Beach (Texas) data of Zimmer et al. (2006). For Poisson's ratio σ the range is selected based on the explanation given in section 2-1 for loose granular material. Depth of inversion is the depth that the data points reaches (Fig. 4-16 and Fig. 4-18).

Table 4-6: Input parameters in the Monte Carlo Inversion for line 1 and 2. The range of the γ_s and σ are given in between the brackets.

	Line 1	Line 2
No. of models	20,000	20,000
No. of layers	12	12
α_s	0.1692 ± 0.0015	0.1963 ± 0.0080
γ_s	[4.5 - 30]	[4.5 - 30]
σ	[0.1 - 0.49]	[0.1 - 0.49]
ρ (kg/m^3)	1560	1560
Depth (m)	1	2.5

The results of the Monte Carlo inversion are shown in figure 4-19, figure 4-20 and Table 4-7 with the results of the power-law coefficients, α_s and γ_S. The V_S profiles of line 1 shown in figure 4-19(a) ranges between ~ 55 m/s and ~ 125 m/s. In addition for line 2, the V_S profiles of line 2 shown in figure 4-20(a) ranges between ~ 40 m/s and ~ 125 m/s. However, the depth reaches deeper than the V_s profile of line 1. Thus, it can be stated that there is clearly not only lateral variation along line 1 investigated in section 4-1-3, but also variation between line 1 and line 2.

Table 4-7: Results of the Monte Carlo Inversion on the power-law coefficients, α_s and γ_s, for line 1 and line 2.

	Line 1	Line 2
α_s	0.1700 ± 0.0003	0.1969 ± 0.0013
γ_s	23.5557 ± 0.0003	16.0933 ± 0.0013

The inverted values for α_s (Table 4-7) are close to the preliminary values with only a maximum difference of three hundredths for line 1. The results of the σ shown in the right plot of figure 4-19(c) and figure 4-20(c) gives no specific value but a spread over the input range due to the absence of higher modes (Bergamo et al. 2013). For both line 1 and line 2, the experimental dispersion curve falls into the minimum of the misfit surface. The comparison between the experimental dispersion curve and the misfit surface are shown in figures 4-19(b) and 4-20(b), for respectively line 1 and line 2.

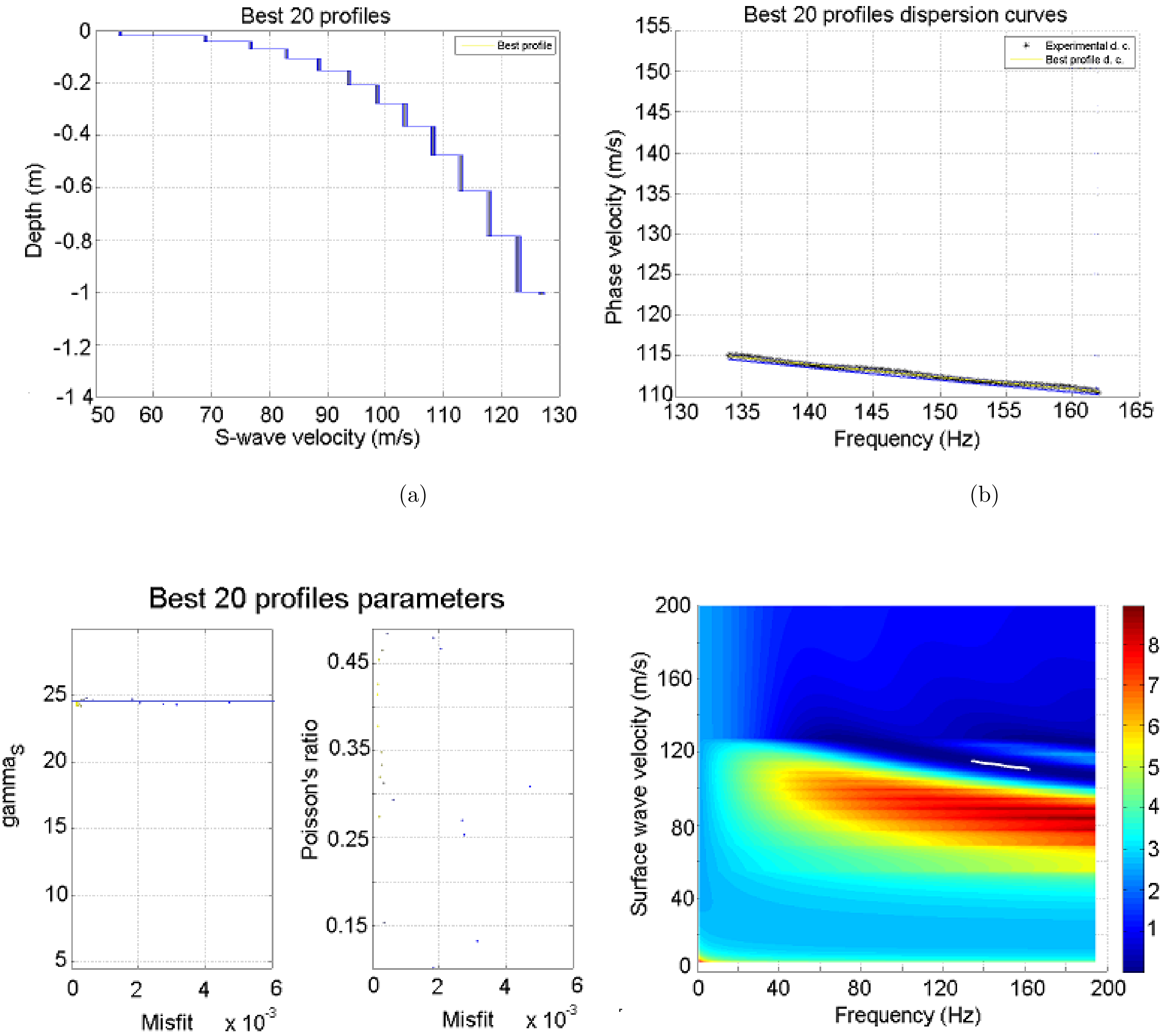

(a) (b)

(c) (d)

Figure 4-19: Monte Carlo inversion results for line 1: a) The 20 best fitting shear-wave velocity models from 20,000 sampled models. b) Best fitting dispersion curves compared with the experimental one. (c) Inversion results for γ_s and σ. d) Real dispersion curve compared with the misfit surface of the determinant approach.

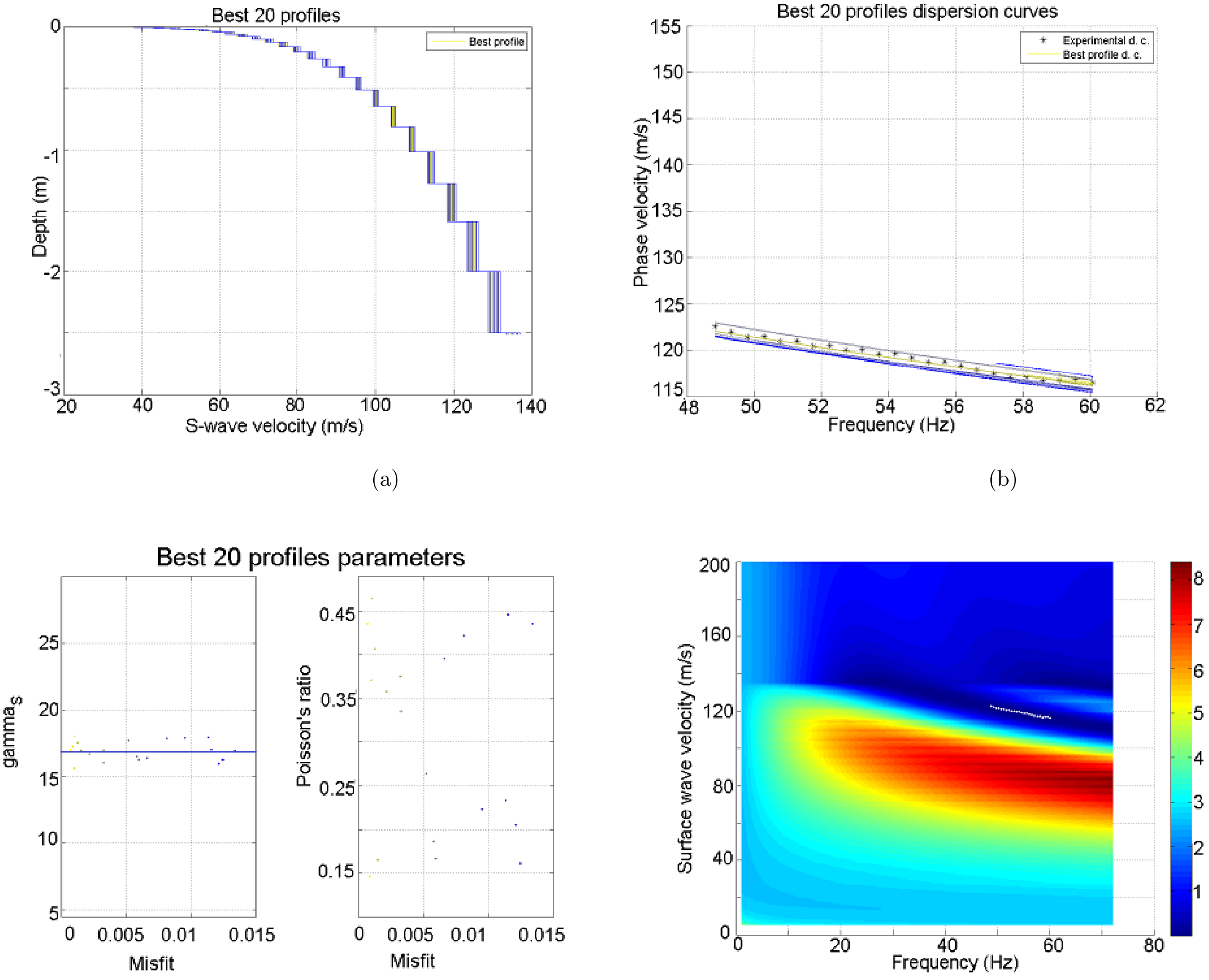

(a)

(b)

(c)

(d)

Figure 4-20: Monte Carlo inversion results for line 2: a) The 20 best fitting shear-wave velocity models from 20,000 sampled models. b) Best fitting dispersion curves compared with the experimental one. (c) Inversion results for γ_s and σ. d) Real dispersion curve compared with the misfit surface of the determinant approach.

Second layer along line 1

From the preliminary alpha estimation along line 1 in section 4-2-2, the data points of the vibroseis data covers two portions that follow a different power-law trend and resulting into two different values for the preliminary alpha. This result can be due to two layers with different properties. Therefore, I will impose a second power-law to the velocity of the second layer V_{s2} and estimate the power-law coefficients belonging to the second layer. The trend of V_{s2} for the second layer will follow a power-law given by:

$$V_{s2} = \gamma_{s2}((\rho_1 g z_1) + (\rho_2 g(z - z_1)))^{\alpha_{s2}} \tag{4-1}$$

where the γ_{s2} and α_{s2} are the power-law coefficients of the second layer, ρ_1 and ρ_2 are respectively the density of the first layer and second layer, z_1 and z are respectively the depth from where the second layer and the depth until where the second power-law holds.

Until z_1 the values for the first layer are fixed, and I use the inversion results given in Table 4-7. The input values of the Monte Carlo inversion on the second layer are given in Table 4-8 together with the results of the estimated power-law coefficients, γ_{s2} and α_{s2}. The results of the Monte Carlo inversion are shown in figure 4-21.

Table 4-8: Input and Output values of the Monte Carlo Inversion performed on the second layer. The range of the γ_{s2} and σ_2 are given in between the brackets.

	Input	Output
No. of models	2000	
No. of layers	12	
α_{s2}	0.2391 ± 0.0051	0.2387 ± 0.7926
γ_{s2}	[4.5 - 30]	9.6682 ± 0.7926
σ_2	[0.1 - 0.49]	-
Density (kg/m^3)	1800	
z_1	1.9	
z (m)	3	

The V_{s2} profiles of the second layer results into velocities ranging between $\sim$ 100 m/s and $\sim$ 450 m/s (Fig. 4-21(a)). The best profiles, lowest misfit, for the second layer results in velocity profiles with lower values than the first layer. For these velocity profiles the data points of the experimental dispersion curve falls into the same local minima of the misfit (Fig. 4-22(b)). And correspond to a γ_{s2} value of $\sim$ 10.

For the V_{s2} profiles with higher velocities than the first layer, the data points of the experimental dispersion curve do not fall into the same local minima of the misfit (Fig. 4-22(a)). Instead the data points belonging to the first layer falls into a local mimima corresponding to a higher surface-wave mode.

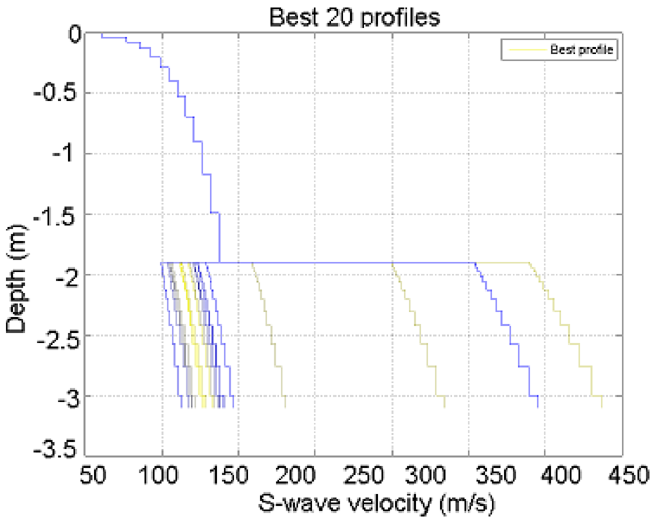

(a)

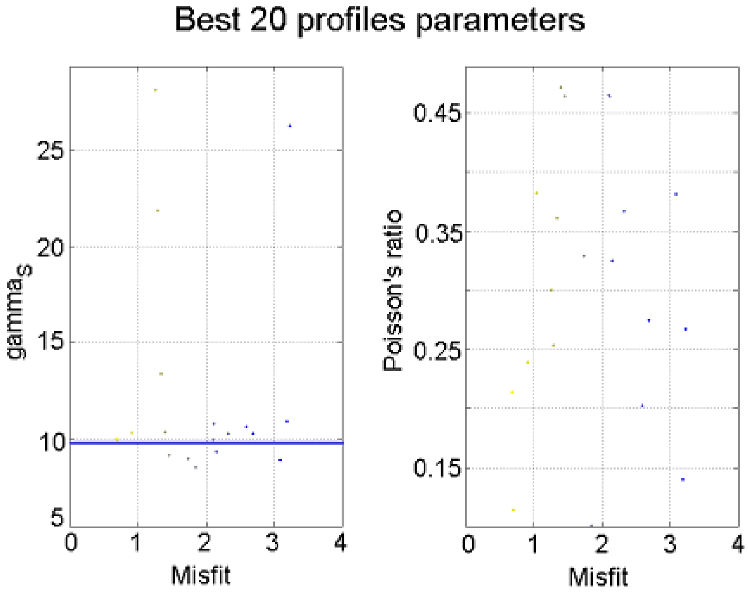

(b)

Figure 4-21: Monte Carlo inversion results of the second layer: a) The 20 best fitting shear-wave velocity models from 20,000 sampled models. b) Inversion results of gamma and Poisson's ratio.

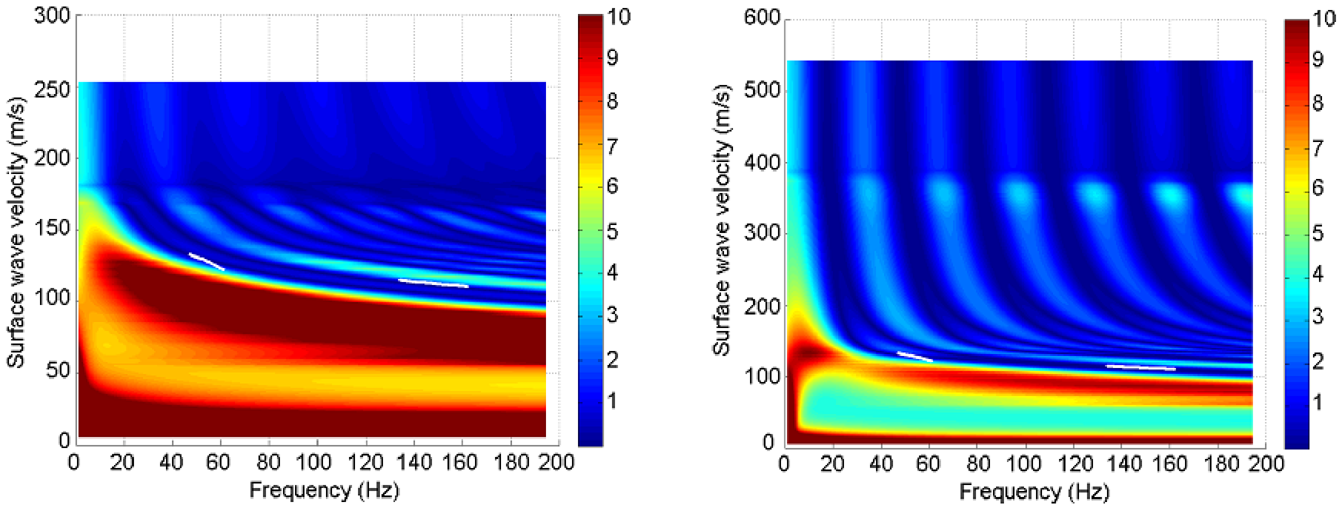

(a) (b)

Figure 4-22: Real dispersion curve compared with the misfit surface of the determinant approach. a) The data points of the first layer falls into the local minima of a higher surface-wave mode. b) The data points of both the first and second layer falls into the same local minima belonging to the first surface-wave mode.

Chapter 5

Discussion

Now that the results are shown, I will explain into more detail their outcomes, the different issues and comparison with the literature values. I will first discuss the outcome of the dispersion curves on their frequency band and lateral variation. Afterwards, I will go into more detail on the P-wave refraction results and the corresponding water-table position. Finally, I will discuss the estimated power-law coefficients and shear-wave velocity profiles. Followed by the problems of inverting for the second layer.

Dispersion Curves

The dispersion curves retrieved from the vibroseis source clearly results into a broader frequency band than the impulsive sources, weight drop and hammer. Thanks to the advantage of the continuous sweep of the vibrating source that covers the whole frequency band in a single signal (Foti et al. 2014). Although there were no significant differences detected between the impulsive sources, I would expect for the weight drop data the energy to be concentrated more in the low frequency band. This is explained by Foti et al. (2014)

that for heavier impulsive sources the energy lies more in the low frequency band.

In addition to the results of the vibroseis data, the dispersion curve retrieved from line 1 with $\Delta x = 0.30$ m (Fig. 4-4) covered a broader frequency range than the other lines (Fig. 4-3 and Fig. 4-6). This can be explained by the length of the array, that was longer than the other two lines thus resulting in a better spectral resolution (Foti et al. 2014).

The Gaussian windowing technique indicates lateral variation along the line, where the dispersion curve corresponding to receiver 41 in figure 4-10 refers to position ∼12 m along the line and the maximum of the Gaussian window. Due to the lateral resolution of 12 m and the maximum of the Gaussian window at ∼12 m, the dispersion curve corresponds to a window range of ∼6 to ∼18 m. Although the presence of lateral resolution was detected a clear identification could not be made in figure 4-10 of the lower velocity region, but the result of figure 4-11 shows a better view on the lower velocity region from 0 to ∼ 7 m along the line.

Water-table position

The P-wave refraction results for the estimation of the water-table position gives for layer 1 and layer 2 respectively $V_p \sim 300$ m/s and $V_p \sim 1420$ m/s. Note that these estimations are not based on a power-law trend like the S-wave velocity, but instead I use a very simple approach of a constant velocity with depth. The P-wave velocity of the first layer falls into the range of the literature values for unconsolidated sands determined by Bachrach et al. (2000). The value P-wave velocity of layer 2: $V_p \sim 1420$ m/s is close to the literature range of Mavko (2005) for wet sand (Table 2-1). With these results it can be said that the refracted layer (layer two) at ∼3 m depth, corresponds to the position of the water-table.

According to the Actueel Hoogtebestand Nederland (AHN) and the maximum-height of the water-table above sea level in the Netherlands coastal dune area, the water-table lies with a minimum depth of 7.2 m and average of 2.2 m below the study area. Thus the inverted depth of the water-table at ∼3 m is in good agreement with these values.

Power-law coefficients and shear-wave velocity

The inverted power-law exponent $\alpha \sim 0.1700$ for line 1 and $\alpha \sim 0.1969$ for line 2 are close to the theoretical values of 1/6 based on perfect spheres with equal size (Walton 1987) and falls into the empirical range of 1/3 - 1/6. These difference are most likely due to the varying shapes of the grains and not the consolidation conditions because the power-law exponent decreases under over-consolidated conditions on average by only 0.01 for the shear-wave velocities (Zimmer et al. 2006). The $\alpha \sim 0.2387$, for the second layer along line 1 is close to the value of the experimental studies in Zimmer et al. (2006), and differs with a maximum ~ 0.07 from the first layer. Also here it can be said that the differences between the first layer and second layer are due to the varying shapes of the grains.

The estimated V_s profiles range between ~ 40 m/s and ~ 125 m/s, which falls into the range 120 ± 60 given by Bachrach et al. (2000); Santamarina et al. (2001). Note that the V_p profiles by assuming a power-law trend to the velocities ,and corresponding power-law coefficients could not be estimated due to the absence of higher surface-wave modes (Bergamo et al. 2013).

The Monte Carlo inverted results on the second portion leads to velocity profiles (Fig. 4-21(a)) in which some corresponds to data points that are assigned to higher surface-wave modes (Fig. 4-22(a)). This assignment is due to the multimodal behavior of the inversion explained in section 2-2-3. However, from the results of the seismic data our experimental data points only correspond to the fundamental surface-wave mode because no higher surface-wave modes were detected. Thus the profiles starting from ~ 200 m/s for the second layer due to data points of the first layer assigned to higher modes, need to be avoided. Furthermore, the experimental points from the second layer do not smoothly fall into the local minima of the misfit surface. The local minima gradually curves upward around 60 Hz where the data points deviate from the local minima. This behavior can be found back into the shear-wave velocity profiles at the beginning of the second portion having a linear behavior and gradually turning into a power-law with depth.

Chapter 6

Conclusions

6-1 Conclusions

For estimation of the shear-wave velocity profile along line 1 and 2, the data from respectively the vibroseis source and weight drop source were selected based on the preliminary results of the alpha. The estimated shear-wave velocity profiles of the sand dune demonstrates the usefulness of imposing a power-law trend to the velocity of the surface waves. The shear-wave velocities falls into the range of the literature values. For the power-law coefficients the estimated values are close to the literature and theoretical values. Nevertheless, the differences with the theoretical value may correspond to differences in the shape of the grains. The estimated shear-wave velocity profiles are limited by the depth of the water-table position, resulting in characterization until the depth of the water-table. The shear-wave velocity profiles of line 1 and 2 are clearly different from each other, because of lateral variation along the lines. The presence of the lateral variation was justified, thanks to the applied Gaussian windowing technique.

Unluckily the computation of the compressional-wave velocity profile and the corresponding power-law coefficients could not be performed due to the absence of higher surface-wave modes in the seismic data. In addition, stacking in the f-k domain resulted in no significant improvement of the spectral resolution in order to detect higher order surface-wave modes

For the second layer, the implementation of the second power-law led to velocity profiles that are higher and lower than the first layer. The higher velocity profiles can be omitted due to the nature of the multimodal behavior of the inversion, that assigned experimental data points to a higher surface-wave mode.

For the best practice in field work I analyzed the data between the lines from the sledgehammer, vibroseis and weight drop data. I would recommend the vibroseis source, because of the broadest and most continuous frequency range for the retrieved dispersion curves. This demonstrates the advantage of the vibrating source that covers the whole frequency band of the sweep in a single signal.

6-2 Outlook

I have shown the usefulness of surface-wave analysis in order to characterize the sand dune, but for a completion of the characterization I would suggest to take samples of the sand along different portions of the line and with varying depth. Laboratory studies on these samples will give insight into the grain size, contact geometry and density. The grain size and contact geometry will be useful information on the accuracy of the power-law coefficients. The density will provide extra information for the corresponding constant value in the Monte Carlo inversion. In addition to velocity profiles reaching a greater depth, an experimental site with a deeper water-table might be more interesting for improvement of the investigation depth.

The implementation of the second-power law into the Monte Carlo inversion is very interesting, yet further work is needed. First, improving the linear behavior of the second layer at the beginning of the shear-wave velocity profiles might lead to a better misfit.

Furthermore, an inversion strategy that assigns the data manually to the mode number can prevent the data from falling into the wrong local minimum.

Bibliography

Aleshin, V., Gusev, V., and Tournat, V. 2007. Acoustic modes propagating along the free surface of granular media. *The Journal of the Acoustical Society of America*, 121(5):2600–2611.

Bachrach, R., Dvorkin, J., and Nur, A. M. 2000. Seismic velocities and poisson's ratio of shallow unconsolidated sands. *Geophysics*, 65(2):559–564.

Bergamo, P. 2012. *Surface wave analysis in laterally varying media.* PhD thesis, Politecnico di Torino.

Bergamo, P., Bodet, L., Socco, L. V., Mourgues, R., and Tournat, V. 2014. Physical modelling of a surface-wave survey over a laterally varying granular medium with property contrasts and velocity gradients. *Geophysical Journal International*, 197(1):233–247.

Bergamo, P., Boiero, D., and Socco, L. V. 2012. Retrieving 2d structures from surface-wave data by means of space-varying spatial windowing. *Geophysics*, 77(4):EN39–EN51.

Bergamo, P., Socco, L. V., et al. 2013. Estimation of p-and s-wave velocity models of unconsolidated granular materials through surface wave multimodal inversion: 83rd annual international meeting, seg. *Expanded Abstracts, doi*, 10.

Bodet, L., Jacob, X., Tournat, V., Mourgues, R., and Gusev, V. 2010. Elasticity profile of an unconsolidated granular medium inferred from guided waves: Toward acoustic monitoring of analogue models. *Tectonophysics*, 496(1):99–104.

Foti, S. 2002. Some notes on model parameters for surface wave data inversion.

Foti, S., Lai, C. G., Rix, G. J., and Strobbia, C. 2014. *Surface wave methods for near-surface site characterization*. CRC Press.

Gabriels, P., Snieder, R., and Nolet, G. 1987. In situ measurements of shear-wave velocity in sediments with higher-mode rayleigh waves. *Geophysical prospecting*, 35(2):187–196.

Gassmann, F. 1951. Elastic waves through a packing of spheres. *Geophysics*, 16(4):673–685.

Ghose, R., Nijhof, V., Brouwer, J., Matsubara, Y., Kaida, Y., and Takahashi, T. 1998. Shallow to very shallow, high-resolution reflection seismic using a portable vibrator system. *Geophysics*, 63(4):1295–1309.

Haskell, N. A. 1953. The dispersion of surface waves on multilayered media. *Bulletin of the seismological Society of America*, 43(1):17–34.

Liner, C. 2007. The seismic sand curve revisited. *Geophysics*, 73(1):A7–A10.

Maraschini, M. and Foti, S. 2010. A monte carlo multimodal inversion of surface waves. *Geophysical Journal International*, 182(3):1557–1566.

Mavko, G. 2005. Conceptual overview of rock and fluid factors that impact seismic velocity and impedance. *Retrieved*, 11(11):2012.

Nazarian, S., Stokoe, I., Kenneth, H., and Hudson, W. 1983. *Use of spectral analysis of surface waves method for determination of moduli and thicknesses of pavement systems.* Number 930.

Park, C. B., Miller, R. D., and Xia, J. 1999. Multichannel analysis of surface waves. *Geophysics*, 64(3):800–808.

Robinson, D. K. and Al-Husseini, M. I. 1982. Technique for reflection prospecting in the rub'al-khali. *Geophysics*, 47(8):1135–1152.

Rossow, J., Applegate, J. K., Keller, G. V., et al. 1983. An attempt to measure poisson's ratio in the subsurface in the geysersclear lake geothermal areas of california. In *1983 SEG Annual Meeting*. Society of Exploration Geophysicists.

Santamarina, J. C., Klein, A., and Fam, M. A. 2001. Soils and waves: Particulate materials behavior, characterization and process monitoring. *Journal of Soils and Sediments*, 1(2):130–130.

Sistermans, P. and Nieuwenhuis, O. 2004. Holland coast (the netherlands).

Socco, L. and Strobbia, C. 2004. Surface-wave method for near-surface characterization: a tutorial. *Near Surface Geophysics*, 2(4):165–185.

Socco, L. V. and Boiero, D. 2008. Improved monte carlo inversion of surface wave data. *Geophysical Prospecting*, 56(3):357–371.

Socco, L. V., Boiero, D., Foti, S., and Wisén, R. 2009. Laterally constrained inversion of ground roll from seismic reflection records. *Geophysics*, 74(6):G35–G45.

Socco, L. V., Foti, S., and Boiero, D. 2010. Surface-wave analysis for building near-surface velocity modelsestablished approaches and new perspectives. *Geophysics*, 75(5):75A83–75A102.

Stokoe, K. H., Wright, S., Bay, J., Roesset, J., et al. 1994. Characterization of geotechnical sites by sasw method. *Geophysical characterization of sites*, pages 15–25.

Thomson, W. T. 1950. Transmission of elastic waves through a stratified solid medium. *Journal of applied Physics*, 21(2):89–93.

Walton, K. 1987. The effective elastic moduli of a random packing of spheres. *Journal of the Mechanics and Physics of Solids*, 35(2):213–226.

Wong, T. E., Batjes, D. A., de Jager, J., and van Wetenschappen, K. N. A. 2007. Geology of the netherlands. Royal Netherlands Academy of Arts and Sciences Amsterdam.

Xia, J., Miller, R. D., and Park, C. B. 1999. Estimation of near-surface shear-wave velocity by inversion of rayleigh waves. *Geophysics*, 64(3):691–700.

Zhang, J. and Toksöz, M. N. 1998. Nonlinear refraction traveltime tomography. *Geophysics*, 63(5):1726–1737.

Zimmer, M. A., Prasad, M., Mavko, G., and Nur, A. 2006. Seismic velocities of unconsolidated sands: Part 1pressure trends from 0.1 to 20 mpa. *Geophysics*, 72(1):E1–E13.